Journal of The Electrochemical Society

The Electrochemical Society
Advancing solid state & electrochemical science & technology

OPEN ACCESS

Temperature and Performance Inhomogeneities in PEM Electrolysis Stacks with Industrial Scale Cells

To cite this article: T. Krenz *et al* 2023 *J. Electrochem. Soc.* **170** 044508

View the article online for updates and enhancements.

You may also like

- Morphological characteristics and productivity of sugar palm saps at several levels of tapping age
D K Wardani, A Junaedi, S Yahya et al.
- Infrastructure performance of irrigation canal to irrigation efficiency of irrigation area of Candi Limo in Mojokerto District
S Kisnanto, R R R Hadiani and C Ikhsan
- Mathematical connection ability of elementary school student in number materials
A K Kenedi, I K Sari, S Ahmad et al.

We Advance Battery Research!

EL-CELL®
electrochemical test equipment

- Electrochemical Battery Test Cells
- Multi-channel Potentiostats / Galvanostats / EIS
- Tools, Consumables & Testing Services

el-cell.com +49 40 79012-734 sales@el-cell.com

This content was downloaded from IP address 89.245.22.244 on 29/09/2023 at 08:16

Journal of The Electrochemical Society, 2023 **170** 044508

Temperature and Performance Inhomogeneities in PEM Electrolysis Stacks with Industrial Scale Cells

T. Krenz,[1,2,=] O. Weiland,[1,=] P. Trinke,[1] L. Helmers,[2] C. Eckert,[1] B. Bensmann,[1,z] and R. Hanke-Rauschenbach[1]

[1]*Electrical Energy Storage Systems, Leibniz Universität Hannover, 30167 Hannover, Germany*
[2]*Siemens Energy Global GmbH & Co. KG, 91058 Erlangen, Germany*

In this work temperature inhomogeneities and their influence on PEMWE performance of industrial-scale stacks are investigated. Three temperature differences are examined: (i) between the inlet and outlet, (ii) in-between the cells of a stack, (iii) between the cell's solid materials and the fluids. A validated stack model for temperature and performance is presented which is used to quantify the above-mentioned temperature fields and their influences on current density distribution and cell voltages. For a chosen scenario, with current densities of 2.0 A cm^{-2}, fluid inlet temperatures of 60 °C and flow-rates of 0.15 kg s^{-1}m^{-2}, peak temperature differences amount to 8.2 K along-the-channel. This relates to inhomogeneities of current density of up to 10% inside a cell and deviations of cell voltage of 9 mV in-between cells in the center of the stack and outer cells. For higher current densities these differences increase further. More homogeneous temperatures allow operation at elevated average temperatures without exceeding temperature limitations and reduce the spread of degradation mechanisms. Hence, homogenous profiles lead to a more hole-some utilization of electrolysis stacks. Therefore, the ability to homogenize via alternative operation such as higher flow-rate, higher pressure and altered routing of fluid-flow is analyzed.

© 2023 The Author(s). Published on behalf of The Electrochemical Society by IOP Publishing Limited. This is an open access article distributed under the terms of the Creative Commons Attribution 4.0 License (CC BY, http://creativecommons.org/licenses/by/4.0/), which permits unrestricted reuse of the work in any medium, provided the original work is properly cited. [DOI: 10.1149/1945-7111/accb68]

Manuscript submitted December 2, 2022; revised manuscript received February 25, 2023. Published April 19, 2023.

Nomenclature

Symbol	Description	Unit/Value
A	Surface Area	m^2
A^{seg}	Active cell area of segment	m^2
b^{a}	Tafel slope on anode side	V
c^i	Concentration of substance i	mol m^{-3}
c_{p}	Specific heat capacity	J kg^{-1}K^{-1}
d	Thickness/Distance	m
D^i	Mass diffusivity for substance i	m^2 s^{-1}
E^i	Activation energy for component i	—
F	Faraday constant	96, 485 C mol^{-1}
ΔG	Gibbs free energy	J kg^{-1}
h^i	Specific enthalpy of species i	J kg^{-1}
H	Enthalpy	J
ΔH	Reaction enthalpy	J kg^{-1}
i	Current density	A m^{-2}
i_0	Exchange current density	A m^{-2}
I	Current	A
k_l	Transport coefficient in catalyst layer	m s^{-1}
K^{mem}	Linear factor for membrane conductivity	Ω m^{-1}
$l_{\text{seg}}^{\text{cell}}$	Length of cell segment	$l_{\text{seg}}^{\text{cell}} = l^{\text{cell}}/N_{\text{seg}}$
m^i	Mass of component i	kg
$\dot{\text{m}}$	Mass flow	kg s^{-1}
M^i	Molar mass of species i	kg mol^{-1}
n_{drag}	Electro-osmotic drag coefficient	22 $\text{mol}_{\text{H}_2\text{O}}$ $\text{mol}_{\text{H}^+}^{-1}$
p	Pressure	Pa
q	Specific heat flux	W m^{-2}

(Continued).

$Q^{\text{s}\to\gamma}$	Heat flow from solid to fluid on γ side	J kg^{-1}
Q^{diss}	Heat generated through voltage losses	J kg^{-1}
R	universal gas constant	8, 314 JK^{-1} mol^{-1}
R^i	Area Specific Ohmic resistance of component i	Ωm^2
S^i	Solubility of substance i	mol m^{-3} Pa^{-1}
S_{V}	Volume specific surface area of heat transfer	m^{2}m^{-3}
T	Temperature	K
ΔT	Temperature difference	K
U^i	Voltage of component i	V
v^i	Fluid velocity on electrode i	m s^{-1}
w^i	Mass fraction of species i	kg kg^{-1}
w^{sat}	Saturation mass fraction	kg kg^{-1}
z	Charge number	—
α^γ	Heat transfer coefficient on γ side	W m^{-2}K^{-1}
$\alpha_{\text{ct}}^\gamma$	Charge transfer coefficient on γ side	—
δ^γ	Thickness of γ side	m
ϵ^γ	Integral porosity of γ side	—
η^i	Overpotential of component i	V
κ_i	Linear factor for calculating the heat transfer coefficient of phase i	—
λ^{sat}	Factor for membrane hydration	—
$\lambda^{k,i}$	Thermal conductivity in direction k of component i	W m^{-1}K^{-1}
σ^{mem}	Membrane ionic conductivity	S m^{-1}
ρ^i	Density of substance i	kg m^{-3}
φ^i	Volume fraction of species i	m^3 m^{-3}

[=]Equal contribution.
[z]E-mail: boris.bensmann@ifes.uni-hannover.de

(Continued).

Superscripts

Symbol	Description	Unit/Value
*	Supersaturation	—
0	Standard state	p = 101, 325 Pa T = 298.15 K
a	Anode or anodic fluid	—
avg	Average	—
c	Cathode or anodic fluid	—
ch	Along-the-channel coordinate	—
con	Contact	—
ct	Charge transfer	—
cs	Cross-sectional	—
ecd	Exchange current density	—
(g)	Gaseous state	—
(l)	Liquid state	—
mem	Membrane	—
mt	Mass transport	—
ref	Reference	—
s	Solid	—
sat	Saturation	—
sc	Stacking coordinate	—
seg	Segment (finite component)	—
rev	Reversible	—
thn	Thermoneutral	—
β	Index for species of fluid	$\beta \in \{H_2O(l), H_2O(g), O_2, H_2\}$
γ	Index for electrode	$\gamma \in$ {Anode, Cathode}

Subscripts

Symbol	Description	Unit/Value
down	Position in along-the-channel coordinate	$j-1$
eff	Effective	—
in	Entering or at inlet of component/segment	—
j	Segment number	$j \in \{1,\ldots,N_{seg}\}$
k	Cell number	$k \in \{1,\ldots,N_{cells}\}$
lat	Lateral	—
left	Position in stacking coordinate	$k-1$
out	Exiting or at outlet of component/segment	—
sens	Sensor	—
sim	Simulation	—
reac	Reaction	—
ref	Reference	—
right	Position in stacking coordinate	$k+1$
up	Position in along-the-channel coordinate	$j+1$

Large-scale water electrolysis projects are currently being planned and implemented.[1] The generation of hydrogen through electrolysis using renewable energy sources is becoming increasingly important due to the current energy and climate crises.[2–4] Large-scale commercial stacks have become available in recent years.[5,6] However, next-gen products provide enormous potential for improvement, with degradation being a major concern.[5,6]

During operation, accelerators for degradation in PEM electrolysis are high temperatures and high current densities.[7,8] This indicates that deviations in temperature and current density within a cell/stack lead to locally different rates of degradation which is why a homogenous distribution of temperature and current density is desirable.[9–11] Measuring temperatures or current densities within a cell or stack is typically not possible in industrial-size plants. Therefore, the local distribution of these values needs to be resolved with models.

The temperature differences inside a stack are caused by heat release in the cells due to voltage losses and heat transfer to the environment at the outer boundaries of the stack as well as convective heat transfer in the fluids. Since the performance of a PEM electrolyzer depends on temperature, the temperature differences inside a stack create local performance inhomogeneities.[10,11] Hence, this inhomogeneity evolves in both, the stacking coordinate as well as the flow direction along-the-channel.

Up to now, model-based analysis of temperature effects is mostly carried out for unstacked, small-scaled laboratory cells, where temperature gradients along-the-channel have minor effects.[12] Onda et al.[13] present an along-the-channel model for a large cell, which is only validated by experimental data for a small cell (10 cm^2 electrode area). Immerz et al.[14] carried out along-the-channel measurements of current density and temperature in a long single-channel setup.

On a stack-level, typically lumped models are used. Olivier et al.[15] validate such a model with experimental data. Another lumped model is used to design a cooling system for a stack.[16] Also, the influence of the operating pressure on anodic and cathodic activation overpotentials is studied with help of a lumped model, which is validated by experimental stack data.[17]

Local diffusive and convective heat transport processes are not addressed in lumped stack models, so local performance differences cannot be observed. Resolving these local differences is important to understand the overall behavior of industrial size stacks. Further effects, such as local degradation, can also only be understood by considering local temperature and performance effects.

In this contribution, we present a validated pseudo-2-D stack model, which addresses the local inhomogeneity predominantly caused by temperature differences within the stack. The model covers two coordinates: the stacking and the along-the-channel coordinate. With help of the model, we calculate local temperatures and their impact on the current densities. Performance differences between cells are discussed at different current densities. Additionally, options to reduce inhomogeneities are studied by varying the operating pressure, the inlet water flow rate, and the water flow arrangement (counter-flow and co-flow).

Model

A schematic of the working principle of a PEM water electrolyzer with the half-cell reactions, the electrodes, the membrane, and the porous transport layers (PTLs) is given in Fig. 1a. The reactions take place within the catalyst layers of the electrolyzer half-cells. In the model, the cells are composed of finite segments, as shown in Fig. 1. In the finite segments of the model, the anodic fluid, the cathodic fluid, and the solid compartment of the segment are balanced separately. The cells are stacked such that they are electrically connected in series and in parallel in regards of the fluid transport (e.g., process water, as it can be seen in Fig. 1).

The model includes three dynamic enthalpy balances to consider temperature dynamics, which are coupled with a quasi-steady state description for the polarization behavior to describe the performance of a rectangular stack. The performance is considered in a quasi-steady state due to the fast dynamics of the charge balances. Even though the dynamic temperature model is used for validation, in the results part, only steady state results are discussed.

The fluid temperatures represent the temperature in each half-cell whereas the solid temperature represents all the solid parts of the corresponding segment (as shown in Fig. 11a) and thereby contains anodic PTL, anodic electrode, membrane, cathodic electrode, cathodic PTL and bipolar plate. Thermal conductivities and heat capacities of the layers are lumped in integrated values covering the layers of the solid compartment. An approach of how to calculate representative parameters for the lumped solid considering the different materials within the solid is given in A·1.

The model is formulated component-based, such that a stack (Fig. 1c) is composed of multiple cells (Fig. 1b), which are formed through multiple segments (Fig. 1a), which are stacked in between

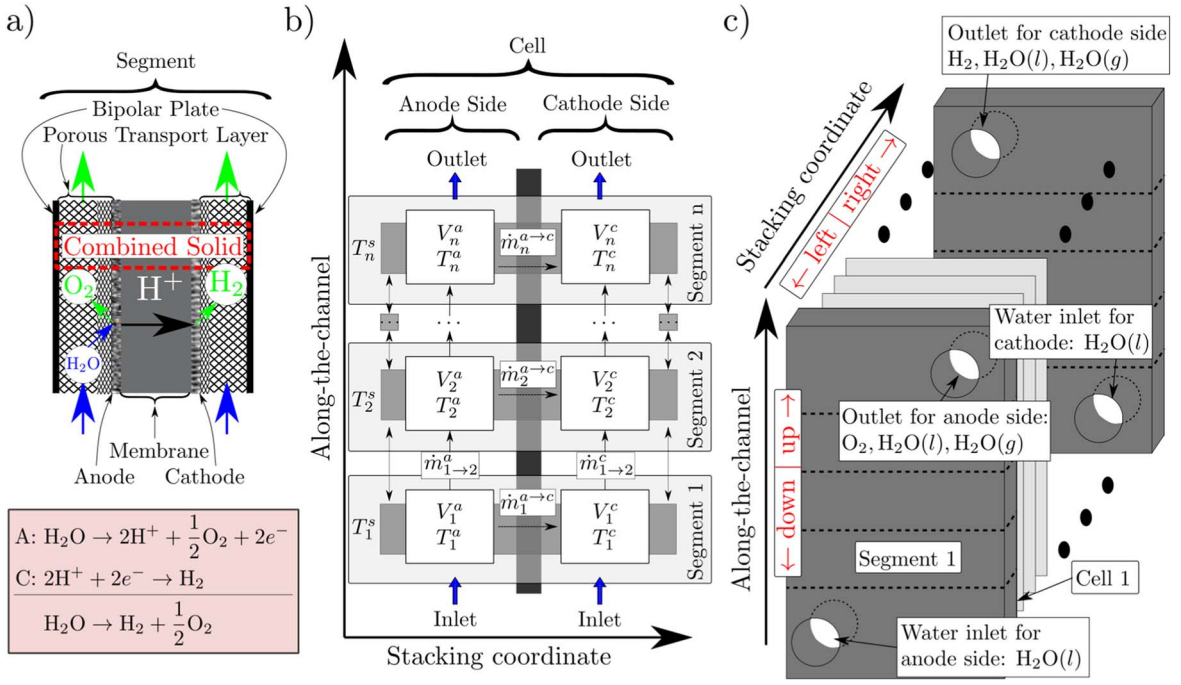

Figure 1. Schematics for working principle of PEMWE, cell model structure and stack. The subfigures are arranged from small to large: (a) the segment, the core component of the model, and basic water electrolysis reaction, (b) the cell model, visualizing the interaction between the model segments and (c) the stack model, showing the used coordinate axis.

two end-plates. The equations describing the stack, the cells, the segments, and its interaction of the hierarchy levels are presented in the following. For simplicity, the use of indexes is limited to a minimum, and neighboring components are referenced by their relative position to the segment (cf. Fig. 1 in along-the-channel coordinate: up/down, in stacking coordinate: left/right).

Segment.—At the lowest level of hierarchy, the segment is the core component of the pseudo-2-D stack model. The behavior of the components is stated from conservation laws and basic polarization behavior.

Enthalpy balances.—Enthalpy balances are formulated for anodic fluid, cathodic fluid and solid. The fluid enthalpy balances are given by:

$$\frac{\mathrm{d}H^{\gamma}}{\mathrm{d}t} = \sum_{\beta} \left(\dot{\mathrm{m}}_{\mathrm{in}}^{\gamma,\beta} h_{\mathrm{in}}^{\gamma,\beta} - \dot{\mathrm{m}}_{\mathrm{out}}^{\gamma,\beta} h_{\mathrm{out}}^{\gamma,\beta}\right) + \dot{Q}^{\mathrm{s}\rightarrow\gamma} \qquad [1]$$

with $\beta \in \{H_2O(l), H_2O(g), O_2\}$ for $\gamma =$ anode and $\beta \in \{H_2O(l), H_2O(g), H_2\}$ for $\gamma =$ cathode. Specific enthalpies $h^{\gamma,\beta}$ are calculated using the Modelica Fluid Library.[18] In this formulation the evaporation enthalpy changes are included implicitly.

The state equations of enthalpy for implicit temperature calculation of the anodic and cathodic fluids are given by:

$$H^{\gamma} = \sum_{\beta} \mathrm{m}^{\gamma,\beta} h^{\gamma,\beta}(T^{\gamma}) \qquad [2]$$

with $\beta \in \{H_2O(l), H_2O(g), O_2\}$ for $\gamma =$ anode and $\beta \in \{H_2O(l), H_2O(g), H_2\}$ for $\gamma =$ cathode.

Liquid and gas phase are assumed to be in a thermal equilibrium. The joint enthalpy balance of all solid components of each segment is given by:

$$\frac{\mathrm{d}H^{\mathrm{s}}}{\mathrm{d}t} = A^{\mathrm{seg}} \cdot (q_{\mathrm{left}}^{\mathrm{sc}} + q_{\mathrm{right}}^{\mathrm{sc}}) + A_{\mathrm{cell}}^{\mathrm{cs}} \cdot (q_{\mathrm{down}}^{\mathrm{ch}} + q_{\mathrm{up}}^{\mathrm{ch}})$$

$$- \dot{Q}^{\mathrm{s}\rightarrow\mathrm{a}} - \dot{Q}^{\mathrm{s}\rightarrow\mathrm{c}} + \dot{Q}^{\mathrm{diss}} \qquad [3]$$

where A^{seg} is the active cell area of the segment and $A_{\mathrm{cell}}^{\mathrm{cs}}$ is the cross-section area of the cell in the along-the-channel coordinate. The indexes sc stand for stacking and ch for along-the-channel coordinate, s for solid, a for anode and c for cathode.

The heat generation $\dot{Q}^{\mathrm{diss}}$ is attributed to the solid. Heat conduction is only accounted within the solid, i.e., fluid heat conduction is neglected compared to convection. The outer surfaces of the cell are thermally insulated, so no additionally heat transfer from the cells' boundaries is considered.

Looking at one specific segment, the heat conduction $q_{\mathrm{left}}^{\mathrm{sc}}$ to its left segment (into a neighboring cell or end-plate respectively) is given by Fourier's law:

$$q_{\mathrm{left}}^{\mathrm{sc}} = \frac{\lambda^{\mathrm{cell,sc}}}{d^{\mathrm{cell}}} \cdot (T_{\mathrm{left}}^{\mathrm{s}} - T^{\mathrm{s}}) \qquad [4]$$

The heat conduction to its right segment $q_{\mathrm{right}}^{\mathrm{sc}}$ (into a neighboring cell or end-plate respectively) is calculated similarly:

$$q_{\mathrm{right}}^{\mathrm{sc}} = \frac{\lambda^{\mathrm{cell,sc}}}{d^{\mathrm{cell}}} \cdot (T_{\mathrm{right}}^{\mathrm{s}} - T^{\mathrm{s}}) \qquad [5]$$

$q_{\mathrm{down}}^{\mathrm{ch}}$ and $q_{\mathrm{up}}^{\mathrm{ch}}$ describe the conductive heat transfer to the segments in along-the-channel coordinate. The heat transfer to the segment above the current segment is given by:

$$q_{\mathrm{up}}^{\mathrm{ch}} = \frac{\lambda^{\mathrm{cell,ch}}}{l_{\mathrm{seg}}^{\mathrm{cell}}} \cdot (T_{\mathrm{up}}^{\mathrm{s}} - T^{\mathrm{s}}) \qquad [6]$$

and heat transfer to the segment below the current segment is calculated similarly:

$$q_{\text{down}}^{\text{ch}} = \frac{\lambda^{\text{ch,cell}}}{l_{\text{seg}}^{\text{cell}}} \cdot (T_{\text{down}}^{\text{s}} - T^{\text{s}}) \quad [7]$$

The temperatures of the neighboring compartments for the along-the-channel coordinate (T_{up}^{s} and $T_{\text{down}}^{\text{s}}$) are set in Ch. 2.2 and for the stacking coordinate ($T_{\text{left}}^{\text{s}}$ and $T_{\text{right}}^{\text{s}}$) in Ch. 2.4.

Heat transfer depends on the phase volume fraction of the fluid. Therefore, the effective heat flux from solid to fluid $\dot{Q}^{\text{s}\to\gamma}$ is divided into contribution of the gas $\dot{Q}^{\text{s}\to\gamma(\text{g})}$ and the liquid phase $\dot{Q}^{\text{s}\to\gamma(\text{l})}$:

$$\dot{Q}^{\text{s}\to\gamma} = \dot{Q}^{\text{s}\to\gamma(\text{g})} + \dot{Q}^{\text{s}\to\gamma(\text{l})} \quad [8]$$

$$\dot{Q}^{\text{s}\to\gamma(\text{g})} = \alpha^{\gamma(\text{g})} S_V^{\gamma} \delta^{\gamma} A^{\text{seg}} \varphi^{\gamma} \cdot (T^{\text{s}} - T^{\gamma}) \quad [9]$$

$$\dot{Q}^{\text{s}\to\gamma(\text{l})} = \alpha^{\gamma(\text{l})} S_V^{\gamma} \delta^{\gamma} A^{\text{seg}} \cdot (1 - \varphi^{\gamma}) \cdot (T^{\text{s}} - T^{\gamma}) \quad [10]$$

The volumetric gas phase fraction φ^{γ} determines the allocation of the heat transfer on gas phase and liquid phase. The fluid temperature is assumed to be equilibrated between liquid and gas phase. The heat transfer coefficients $\alpha^{\gamma(\text{g})}$ and $\alpha^{\gamma(\text{l})}$ are functions of the fluid velocity, with a volume specific heat transfer area S_V^{γ}.

$$a^{\gamma(\text{l/g})} = \kappa_{\text{l/g}} \, |v^{\gamma}|^{0.85} \quad [11]$$

Equation 11 is adapted from an approach of the VDI-Wärmeatlas[19] (VDI-heat-atlas). Due to the lack of adequate literature on this kind of heat transfer in porous layers inside structures of PTLs, the approach can only be considered as an approximation and a proposal for a simple description of the heat transfer problem. This approach is fitted, such that the results agree with the found temperature differences between solid and fluid of Onda et al.[13] The linear factor $\kappa_{\text{l/g}}$ is set to a value one order of magnitude larger in the liquid case compared to the gaseous case.

Heat is generated through cell voltages above the thermoneutral voltage:

$$\dot{Q}^{\text{diss}} = A^{\text{seg}} i \cdot (U^{\text{cell}} - U^{\text{thn}}) \quad [12]$$

where i is the segment's current density, U^{cell} is the cell voltage which is invariant of the along-the-channel coordinate in each cell and therefore calculated in the cell's performance model (cf. Ch. 2.1.3), and U^{thn} is the thermoneutral voltage.

The state equation for implicit temperature calculation is given by:

$$H^{\text{s}} = m^{\text{s}} c_p^{\text{cell}} T^{\text{s}} \quad [13]$$

$m^{\text{s}} c_p^{\text{cell}}$ is the total heat capacity of the solids in the cell segment, consisting of various materials and sizes.

Mass balances.—Two mass balances are formulated on each half-cell: One mass balance for water and one for the product-gas.

Water balances.—The local water mass balance is set up for the liquid and gaseous phase together.

$$\frac{\text{d}m^{\gamma,\text{H}_2\text{O}}}{\text{d}t} = \dot{m}_{\text{in}}^{\gamma,\text{H}_2\text{O}} - \dot{m}_{\text{out}}^{\gamma,\text{H}_2\text{O}} - \dot{m}_{\text{reac}}^{\gamma,\text{H}_2\text{O}} \pm \dot{m}_{\text{drag}}^{\text{H}_2\text{O}} \quad [14]$$

$\dot{m}_{\text{in}}^{\gamma,\text{H}_2\text{O}}$ and $\dot{m}_{\text{out}}^{\gamma,\text{H}_2\text{O}}$ are the incoming and outgoing mass fluxes, $\dot{m}_{\text{reac}}^{\text{H}_2\text{O}}$ is the reaction sink term and $\dot{m}_{\text{drag}}^{\text{H}_2\text{O}}$ the water drag which goes from the anode to cathode side.

The incoming and outgoing water mass flux consist of liquid and gaseous water:

$$\dot{m}_{\text{in}}^{\gamma,\text{H}_2\text{O}} = \dot{m}_{\text{in}}^{\gamma} \cdot (w_{\text{in}}^{\gamma,\text{H}_2\text{O(g)}} + w_{\text{in}}^{\gamma,\text{H}_2\text{O(l)}}) \quad [15]$$

$$\dot{m}_{\text{out}}^{\gamma,\text{H}_2\text{O}} = \dot{m}_{\text{out}}^{\gamma} \cdot (w_{\text{out}}^{\gamma,\text{H}_2\text{O(g)}} + w_{\text{out}}^{\gamma,\text{H}_2\text{O(l)}}) \quad [16]$$

The mass fraction of a species is calculated with Eq. 17:

$$w_{\text{out}}^{\gamma,\beta} = \frac{m^{\gamma,\beta}}{\sum_{\beta} m^{\gamma,\beta}} \quad [17]$$

For water, the reaction takes place only on the anode side, which gives Eq. 18:

$$\dot{m}_{\text{reac}}^{\text{a,H}_2\text{O}} = \frac{i A^{\text{seg}}}{2F} M^{\text{H}_2\text{O}} \quad [18]$$

where $M^{\text{H}_2\text{O}}$ is the molar mass of water. Electro-osmotic drag is calculated with the approach of Springer et al.[20] whereas a liquid-water saturated membrane ($\lambda = 22$) is assumed:[21]

$$\dot{m}_{\text{drag}}^{\text{H}_2\text{O}} = M^{\text{H}_2\text{O}} n_{\text{drag}} \frac{i A^{\text{seg}}}{\text{F}} \quad [19]$$

Here, n_{drag} is the drag coefficient.

Product gas balances.—The product-gas is balanced similarly to water:

$$\frac{\text{d}m^{\gamma,\text{H}_2/\text{O}_2}}{\text{d}t} = \dot{m}_{\text{in}}^{\gamma,\text{H}_2/\text{O}_2} - \dot{m}_{\text{out}}^{\gamma,\text{H}_2/\text{O}_2} + \dot{m}_{\text{reac}}^{\gamma,\text{H}_2/\text{O}_2} \quad [20]$$

The outlet mass flow of the product-gas is calculated with help of the mass fraction $w_{\text{out}}^{\gamma,\text{H}_2/\text{O}_2}$ in each segment:

$$\dot{m}_{\text{out}}^{\gamma,\text{H}_2/\text{O}_2} = \dot{m}_{\text{out}}^{\gamma} w_{\text{out}}^{\gamma,\text{H}_2/\text{O}_2} \quad [21]$$

Where $\dot{m}_{\text{out}}^{\gamma}$ is the total mass flow leaving the segment in half-cell γ.

The product-gas production is calculated with Faraday's law:

$$\dot{m}_{\text{reac}}^{\gamma,\text{O}_2/\text{H}_2} = \frac{i A^{\text{seg}}}{z\text{F}} M^{\text{O}_2/\text{H}_2} \quad [22]$$

The mass of the gaseous water is given by:

$$m^{\gamma,\text{H}_2\text{O(g)}} = w^{\gamma,\text{sat}} m^{\gamma,\text{O}_2/\text{H}_2} \quad [23]$$

Here, $w^{\text{sat},\gamma}$ is the saturated mass fraction of gaseous water in hydrogen and oxygen respectively:

$$w^{\gamma,\text{sat}} = \frac{M^{\text{H}_2\text{O}}}{M^{\text{O}_2/\text{H}_2}} \cdot \frac{p^{\gamma,\text{sat}}(T^{\gamma})}{p - p^{\gamma,\text{sat}}(T^{\gamma})} \quad [24]$$

The saturation pressure $p^{\gamma,\text{sat}}(T^{\gamma})$ is taken from the Modelica Fluid Library.[18] Water-saturated gases are assumed within Eqs. 23 and 24, so water evaporates immediately with product gas formation. The evaporation enthalpy is considered within Eq. 1.

Liquid water fills the volume, which is not blocked by gas:

$$m^{\gamma,\text{H}_2\text{O(l)}} = \rho^{\gamma,\text{H}_2\text{O(l)}}(T^{\gamma}) \epsilon^{\gamma} \delta^{\gamma} A^{\text{seg}} \cdot (1 - \varphi^{\gamma}) \quad [25]$$

The gaseous volume fraction φ^{γ} is calculated treating the gas as ideal:

$$\varphi^{\gamma} = \frac{\text{R}T^{\gamma}}{p \epsilon^{\gamma} \delta^{\gamma} A^{\text{seg}}} \cdot \left(\frac{m^{\gamma,\text{H}_2\text{O(g)}}}{M^{\text{H}_2\text{O}} p} + \frac{m^{\gamma,\beta}}{M^{\beta} p} \right) \quad [26]$$

Polarization behavior.—The contributions to the cell voltage are calculated in each segment where again the use of indexes is avoided when possible. All contributions to the cell voltage are segment specific, whereas the cell voltage of segments of a cell are equal (cf. Ch. 2.2).

$$U^{\text{cell}} = U^{\text{rev}} + \eta^{\text{act,a}} - \eta^{\text{act,c}} + i\cdot(R^{\text{mem}} + R^{\text{con}}) + \eta^{\text{mt}} \quad [27]$$

U^{rev} is the reversible cell voltage, i is the current density, $\eta^{\text{act,a}}$ and $\eta^{\text{act,c}}$ are the anodic and cathodic activation overpotentials, R^{mem} is the ionic membrane resistance and R^{con} the contact resistance contributing to the ionic and ohmic losses respectively, and η^{mt} is the mass transfer overpotential.

Reversible cell potential.—is calculated with the Nernst-equation.[22]

$$U^{\text{rev}} = U^{\text{rev},0} + \frac{\text{R}T^{\text{s}}}{2\text{F}} \ln\left(\frac{c^{\text{c,H}_2,\text{sat}}}{c^{\text{c,H}_2,0}} \cdot \left(\frac{c^{\text{a,O}_2,\text{sat}}}{c^{\text{a,O}_2,0}}\right)^{\frac{1}{2}}\right) \quad [28]$$

$U^{\text{rev},0}$ is the reversible cell potential under standard conditions, $c^{\gamma,\text{O}_2/\text{H}_2,\text{sat}}$ are the saturation concentrations at operating conditions and $c^{\gamma,\text{O}_2/\text{H}_2,0}$ at standard conditions.

The reversible potential under standard conditions is calculated with the Gibbs free energy ΔG^0 under standard conditions, which is calculated as follows:

$$U^{\text{rev},0} = -\frac{\Delta G^0}{2\text{F}} \quad [29]$$

$$\Delta G^0 = G^{\text{H}_2,0} + \frac{1}{2} G^{\text{O}_2,0} - G^{\text{H}_2\text{O},0}$$

$$= H^{\text{H}_2,0} + \frac{1}{2} H^{\text{O}_2,0} - H^{\text{H}_2\text{O},0} - T^0 \cdot \left(S^{\text{H}_2,0} + \frac{1}{2} S^{\text{O}_2,0} - S^{\text{H}_2\text{O},0}\right) \quad [30]$$

The saturation concentrations in Eq. 28 are calculated using Henry's law:

$$c^{\gamma,\text{O}_2/\text{H}_2,0} = p^0 S^{\gamma,\text{O}_2/\text{H}_2,0} \quad [31]$$

$$c^{\gamma,\text{O}_2/\text{H}_2,\text{sat}} = p S^{\gamma,\text{O}_2/\text{H}_2,\text{sat}} \quad [32]$$

The Henry constant $S^{\gamma,\text{O}_2/\text{H}_2,\text{sat}}$ depends on temperature, as published by Ito et al.[23]

Thermoneutral voltage.—is calculated with the free enthalpy ΔH:

$$U^{\text{thn}} = -\frac{\Delta H(T^s)}{2\text{F}} \quad [33]$$

$\Delta H(T^s)$ is calculated with the enthalpies of the educts and products:[18]

$$\Delta H(T^s) = H^{\text{H}_2}(T^s) + \frac{1}{2} H^{\text{O}_2}(T^s) - H^{\text{H}_2\text{O}}(T^s) \quad [34]$$

Kinetic losses.—The activation overpotential of the anode is calculated using Tafel kinetics:

$$\eta^{\text{act,a}} = b^{\text{a}} \ln\left(\frac{i}{i_0^{\text{a}}}\right) \quad [35]$$

where b^{a} is the Tafel slope, i the segment's current density and i_0^{a} the anodic exchange current density. The Tafel slope is given by:

$$b^{\text{a}} = \frac{\text{R}\cdot T^{\text{s}}}{2\alpha_{\text{ct}}^{\text{a}}\text{F}} \quad [36]$$

where α_{ct}^{a} is the temperature dependent charge transfer coefficient, which is calculated with an Arrhenius approach to consider temperature effects:[24]

$$\alpha_{\text{ct}}^{a} = \alpha_{\text{ct}}^{a,\text{ref}} \exp\left(E^{\text{ct}} \cdot \left(\frac{1}{333.15\ \text{K}} - \frac{1}{T^{\text{s}}}\right)\right) \quad [37]$$

$\alpha_{\text{ct}}^{a,\text{ref}}$ is the reference charge transfer coefficient at 333.15 K and E^{ct} is the activation energy.

The temperature dependent anodic exchange current density is also calculated with an Arrhenius approach:[25]

$$i_0^{\text{a}} = i_0^{\text{a,ref}} \exp\left(\frac{E^{\text{acd}}}{R} \cdot \left(\frac{1}{353.15\text{K}} - \frac{1}{T^{\text{s}}}\right)\right) \quad [38]$$

Here, $i_0^{a,\text{ref}}$ is the reference exchange current density at 353.15 K and E^{acd} is the activation energy. The cathodic activation overpotential $\eta^{\text{act,c}}$ is neglected, as its contribution of the overall activation overpotentials is small:

$$\eta^{\text{act,c}} = 0 \quad [39]$$

Ohmic losses.—have two components: An ionic membrane resistance and a contact resistance:

$$\eta^{\text{ohm}} = i\cdot(R^{\text{mem}} + R^{\text{con}}) \quad [40]$$

R^{mem} is the ionic membrane resistance and R^{con} is the contact resistance. R^{mem} is given by:

$$R^{\text{mem}} = \frac{\sigma^{\text{mem}}}{\delta^{\text{mem}}} \quad [41]$$

with membrane thickness δ^{mem}. The membrane conductivity σ^{mem} is calculated with the approach of Springer et al.:[20]

$$\sigma^{\text{mem}} = (K^{\text{mem}}\lambda^{\text{sat}} - 0.326)\cdot\exp\left(E^{\text{mem}} \cdot \left(\frac{1}{303\ \text{K}} - \frac{1}{T^{\text{s}}}\right)\right) \quad [42]$$

K^{mem} is a linear factor determining the membrane conductivity, $\lambda^{\text{sat}} = 22$ is the water content of the membrane,[21] and E^{mem} is the activation energy.

Constant contact resistance is assumed with $R^{\text{con}} = 4.3\cdot10^{-6}\ \ \Omega\text{m}^2$.[26]

Mass transfer losses.—These overpotentials evolve because of mass transfer resistances out of the catalyst layer and result in supersaturated gas concentrations inside these catalyst layers. They are calculated with the Nernst equation:[27]

$$\eta^{\gamma,\text{mt}} = \frac{\text{R}T^{\gamma}}{2\text{F}} \ln\left(\frac{c^{\text{a,O}_2,*}}{c^{\text{a,O}_2,\text{sat}}}\right)^{\frac{1}{2}} + \frac{\text{R}T^{\text{c}}}{2\text{F}} \ln\left(\frac{c^{\text{c,H}_2,*}}{c^{\text{c,H}_2,\text{sat}}}\right) \quad [43]$$

Where $c^{\text{a,O}_2,*}$ and $c^{\text{c,H}_2,*}$ are the supersaturation concentrations, which arises because of the mass transfer resistances.

$$c^{\gamma,\text{O}_2/\text{H}_2,*} = \frac{\frac{i}{2\text{F}} + k_l \ \ c^{\gamma,\text{O}_2/\text{H}_2,\text{sat}}}{k_l + \frac{D^{\text{O}_2/\text{H}_2}}{\delta^{\text{mem}}}} \quad [44]$$

k_l is the mass transfer coefficient,[28] $D^{\text{O}_2/\text{H}_2}$ is the diffusivity of oxygen and hydrogen respectively inside the PEM, which are calculated with the approach of Wu et al.[29]

Cell.—Cells are composed of segments that are connected in the along-the-channel coordinate. The segments of a cell interact via charge balances, mass balances and energy balances.

The mass balances are rather simple. The outlet mass flow rate and state of one segment equal the inlet mass flow rate and state of the upper segment in along-the-channel direction. Additionally, the

Table I. Parameters used to define the pseudo-2D stack model.

Symbol	Description	Unit/Value	Source/Material
A^{cell}	Active cell area	1.0 m^2	
$A^{\text{cs}}_{\text{cell}}$	Cross sectional area of cell in along-the-channel coordinate	$a^{\text{cell}} \cdot d^{\text{cell}}$	
$A^{\text{cs}}_{\text{ep}}$	Cross sectional area of end-plate in along-the-channel coordinate	$a^{\text{ep}} \cdot d^{\text{ep}}$	
$A^{\text{ep}}_{\text{lat}}$	Outer lateral surface area of end-plate segment	2.0 m^2	
$A^{\text{ep}}_{\text{top}}$	Outer surface area at top of end-plate segment	0.025 m^2	
a^{cell}	Width cell	0.50m	
a^{ep}	Width end-plate	0.54m	
c_p^{cell}	Specific heat capacity (cell segment)	523J $kg^{-1}K^{-1}$	[19]/Titanium
c_p^{ep}	Specific heat capacity end-plate	470J $kg^{-1}K^{-1}$	[19]/Stainless steel
$d^{\text{cell}-\text{ep}}$	Distance between cell segment and end-plate segment for describing conductive heat transport in stacking direction	0.05m	
d^{cell}	Thickness of cell	$\delta^a + \delta^c$	
d^{ep}	Thickness of end-plate	0.05m	
E^{ct}	Activation energy for charge transfer coefficient	510	Fitting
E^{acd}	Activation energy for exchange current density	4, 300	25
E^{mem}	Activation energy for membrane conductivity	1, 268	20
h^{cell}	Height of cell	2.0m	
$i_0^{a,\text{ref}}$	Anodic reference exchange current density at $T = 353.15K$	$8.0 \cdot 10^{-5}$ A m^2	25
K^{mem}	Factor for membrane conductivity	0.5139 Ω m^{-1}	20
k_l	Transport coefficient in catalyst layer	0.01ms^{-1}	28
$l^{\text{cell}}_{\text{seg}}$	Length of cell segment	$l^{\text{cell}}_{\text{seg}} = l^{\text{cell}}/N_{\text{seg}}$	
l^{ep}	Height of end-plate	2.20m	
m^{cell}	Mass of cell	50kg	
m^{ep}	Mass of end-plate	460kg	
m^{s}	Mass of solid compartment of cell segment	$m^{\text{cell}}/N_{\text{seg}}$	
N_{cells}	Number of cells	40	
N_{seg}	Number of segments	10	
R^{con}	Contact resistance	$4.3 \cdot 10^{-6}$ Ωm^2	26
S_v^a	Volume specific surface (Anode)	180m^2m^{-3}	
S_v^c	Volume specific surface (Cathode)	180m^2m^{-3}	
$\alpha^{\text{ep}}_{\text{top}}$	Heat transfer coefficient for horizontal surface at top of end-plate	185W $m^{-2}K^{-1}$	19
$\alpha^{\text{ep}}_{\text{lat}}$	Heat transfer coefficient for lateral surface of end-plates	45W $m^{-2}K^{-1}$	19
$\alpha^{\text{a,ref}}_{\text{ct}}$	Anodic reference charge transfer coefficient at $T = 333.15K$	0.50	25
δ^a	Thickness of anode half of cell (anodic PTL + half of MEA and half of bipolar plate)	$6 \cdot 10^{-3}$ m	—
δ^c	Thickness of cathode half of cell (cathodic PTL + half of MEA and half of bipolar plate)	$6 \cdot 10^{-3}$ m	—
δ^{mem}	Thickness of membrane	100μm	—
ϵ^a	Integral porosity of anodic PTL	0.60	—
ϵ^c	Integral porosity of cathodic PTL	0.60	—
κ_l	Heat transfer factor solid to liquid fluid	15, 000W $m^{-2}K^{-1}$	Fitted with [13,19]
κ_g	Heat transfer factor solid to gaseous fluid	1, 500W $m^{-2}K^{-1}$	Fitted with [13,19]
$\lambda^{\text{cell,ch}}$	Thermal conductivity (along-the-channel)	8.3W$m^{-1}K^{-1}$	Calculation: appendix Eq. A·1

Table I. (Continued).

Symbol	Description	Unit/Value	Source/Material
$\lambda^{cell,sc}$	Thermal conductivity (stacking coordinate)	$7.56 Wm^{-1}K^{-1}$	Calculation: appendix Eq. A2)
λ^{ep}	Thermal conductivity (end-plate)	$15 Wm^{-1}K^{-1}$	[19]/Stainless steel
$\lambda^{ep,cell}$	Thermal conductivity (end-plate to cell)	$13.57\ Wm^{-1}K^{-1}$	Calculation: appendix Eq. A·3
λ^{sat}	Saturated liquid water content in membrane	22	21

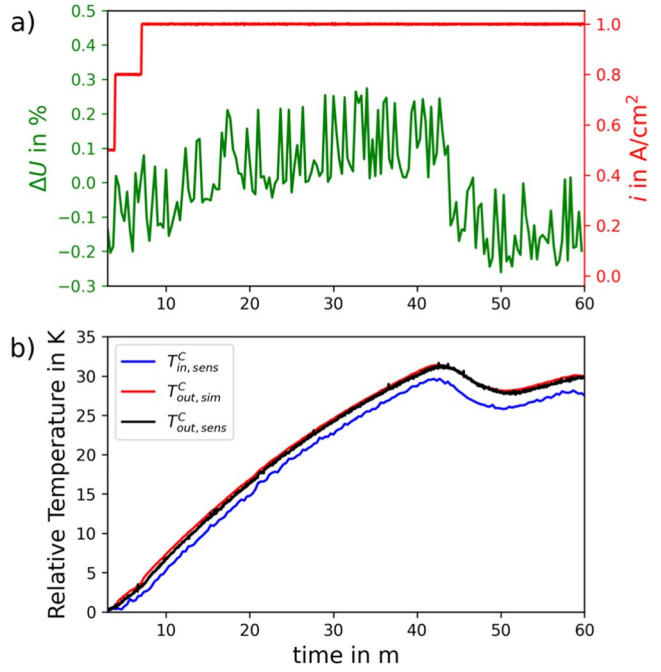

Figure 2. Model validation at cold start of stack to partial load of 1.0 A cm^{-2}: (a) current density (red) and relative error in simulated voltage $\Delta U = (U_{sim} - U_{sens})/U_{sens}$ in % (green) and (b) measured fluid temperature increase since cold start at inlet and outlet of cathode side ($T^c_{in,sens}$, $T^c_{out,sens}$) and corresponding simulated fluid temperature ($T^c_{out,sim}$).

operation pressure p is assumed to be invariant of the along-the-channel coordinate.

Energy balances.—The conductive heat transport within a cell is formulated within every segment (cf. Eqs. 4–7) and is defined by the temperatures of the neighboring segments. For the neighboring temperatures along-the-channel this is done in the cell model.

Since at the top segment of a cell no upper solid temperature exists and the heat transfer in this direction out of the segment needs to be zero, the upper temperature T^s_{up} is set to T^s:

$$T^s_{j,up} = \begin{cases} T^s_{j+1} & \text{for } j \in \{1 \text{ to } N_{seg} - 1\} \\ T^s_j & \text{for } j = N_{seg} \end{cases} \quad [45]$$

For the bottom segment, the reference temperature is set similarly:

$$T^s_{j,down} = \begin{cases} T^s_{j-1} & \text{for } j \in \{2 \text{ to } N_{seg}\} \\ T^s_j & \text{for } j = 1 \end{cases} \quad [46]$$

Charge balances.—Quasi-stationary conditions are assumed, as the dynamics within the double layer are neglected in this work. The cell current splits up in the segment current which gives:

$$I^{cell} = \sum_{j=1}^{N_{seg}} i_j \quad A^{seg} \quad [47]$$

where i_j is the current density of segment j in the cell and A^{seg} is the active cell area of the segment.

A high electric conductivity of the bipolar plate is assumed. This leads to negligible voltage losses inside a bipolar plate and to uniform cell voltage in all segments of one cell:

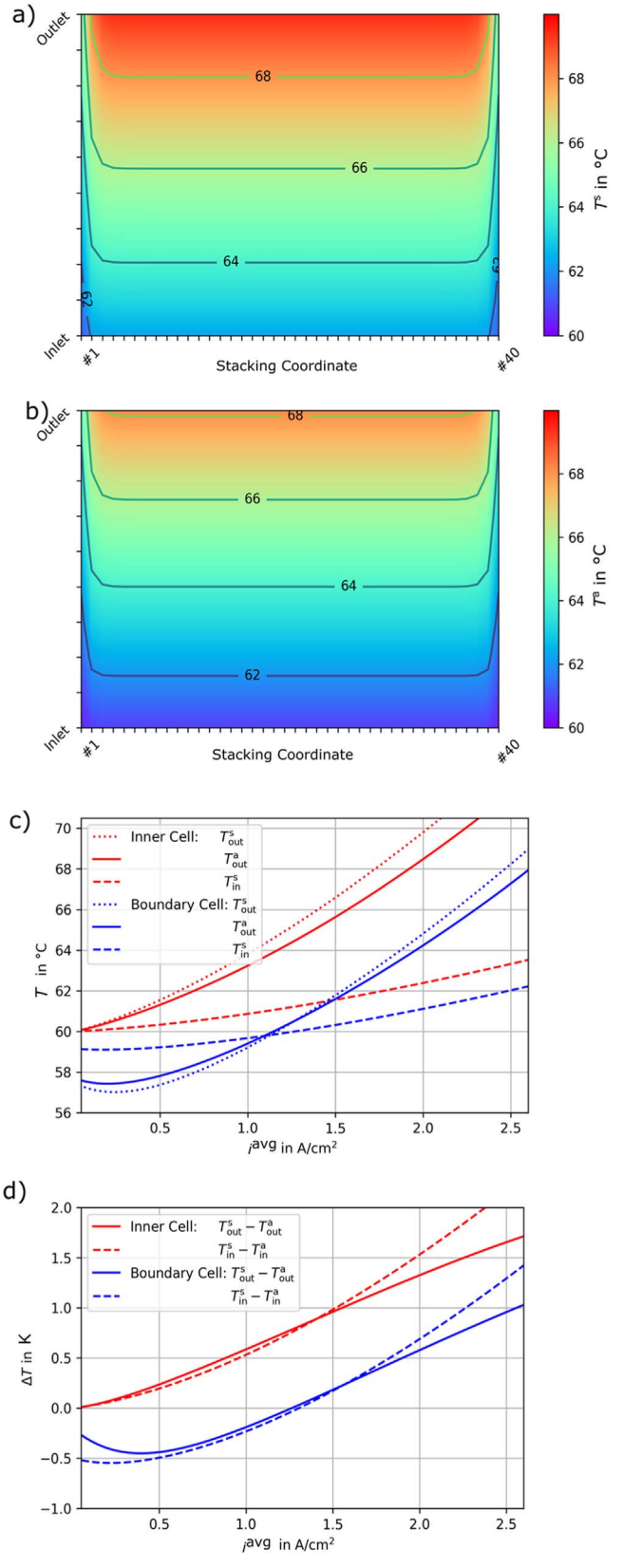

Figure 3. Temperature curves with inlet fluid temperatures of 60 °C and average current density of 2.0 A cm^{-2}: (a) solid temperature T^s inside the stack, (b) anodic fluid temperature T^a inside the stack, (c) absolute temperatures at specific locations mapped over different current densities and d) temperature differences between anodic fluid and solid temperature over different current densities.

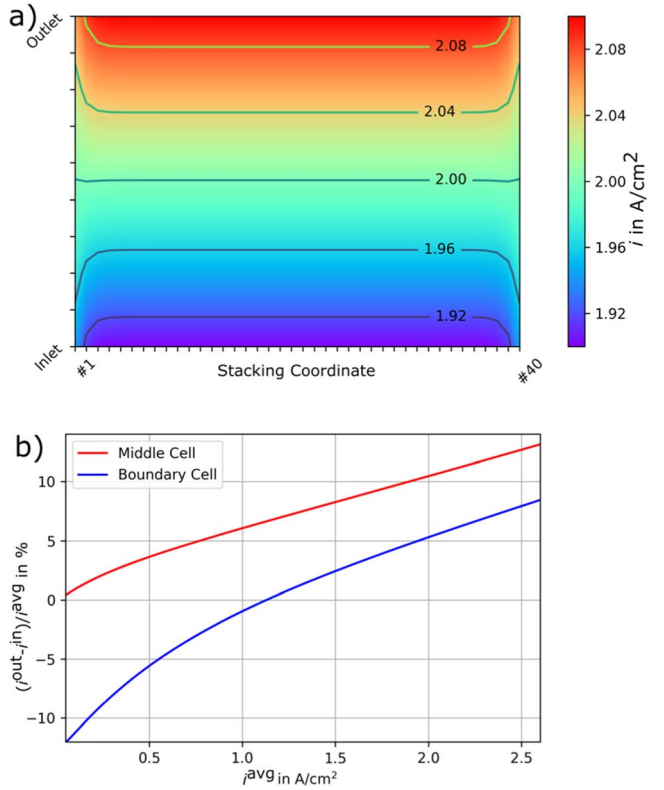

Figure 4. (a) current density distribution of the stack at an average current density of 2.0 A cm^{-2} and (b) difference between inlet and outlet current density for the boundary and a representative middle cell.

$$U^{\text{cell}} = U_j^{\text{seg}} \; \forall \, j \in \{1,\ldots,N_{\text{seg}}\} \qquad [48]$$

Since the loss mechanisms within a cell depend on temperature (cf. Ch. 2.1.3), for every segment of a cell to reach its cell voltage, the current density within every segment must adopt accordingly.

End-plate.—The end-plates of the stack cover the left and right boundaries of the stack. These end-plates are discretized in the along-the-channel coordinate.

The end-plate consists of N_{seg} finite segments. In the following, the equations describing one segment of the end-plate and its interaction with the neighboring end-plate segments (up and down) and the neighboring cell segment (left and right) are given (cf. Fig. 1).

Energy balances.—On one side, the outer surfaces of the end-plates interact with the surrounding air. On the other side, the end-plate is thermally coupled with the boundary cells (cf. Fig. 1).

Because of the lack of mass transfer inside the end-plate, a temperature-based energy balance is used instead of an enthalpy balance:

$$\frac{m^{\text{ep}}}{N_{\text{seg}}} c_p^{\text{ep}} \frac{\mathrm{d}T^{\text{ep}}}{\mathrm{d}t} = \dot{Q}^{\text{cell}\to\text{ep}} + \dot{Q}^{\text{ep,ch}} - \dot{Q}_{\text{eff}}^{\text{ep}\to\text{amb}} \qquad [49]$$

N_{seg} is the number of segments, as the end-plate is discretized in along-the-channel coordinate, c_p^{ep} is specific heat capacity of the end-plate, T^{ep} is the segment specific temperature of the end-plate, $\dot{Q}^{\text{cell}\to\text{ep}}$ is the heat transport between end-plate and boundary cell, $\dot{Q}^{\text{ep,ch}}$ is the heat transport in along-the-channel direction and $\dot{Q}^{\text{ep}\to\text{amb}}$ is the heat transfer between end-plate and surrounding air.

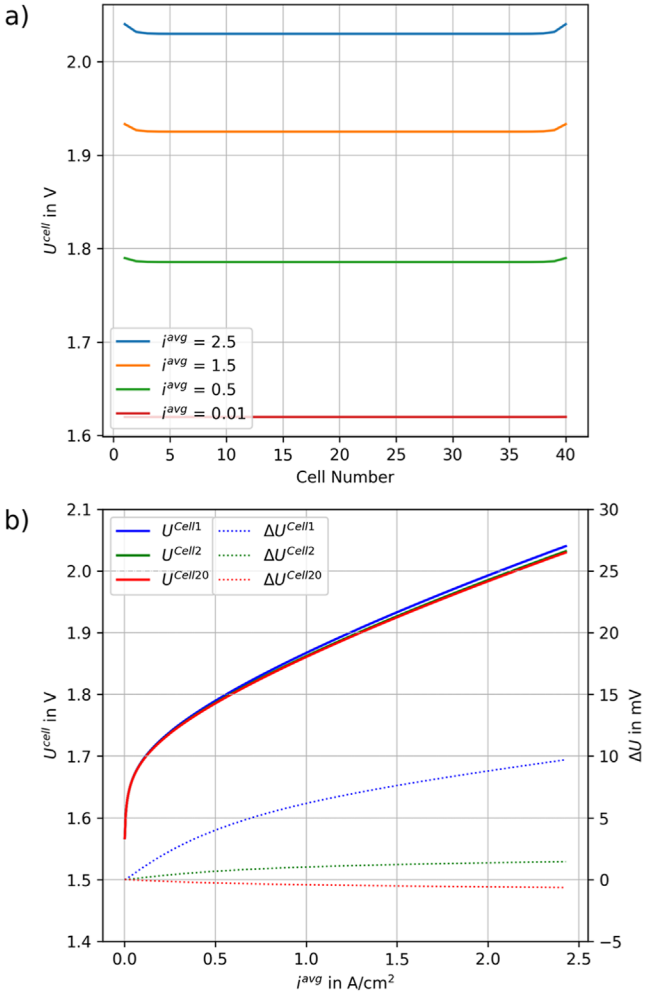

Figure 5. Polarization behavior: (a) cell voltages over stack coordinate for different current densities in A cm^{-2} and (b) polarization curves of different cells (solid lines, in V) and deviations from avg. stack voltage (dotted lines, in mV).

Between end-plate segment and the solid of the neighboring cell the heat transport follows Fourier's law:

$$\dot{Q}^{\text{cell}\to\text{ep}} = \frac{\lambda^{\text{ep,cell}}}{d^{\text{cell}-\text{ep}}} A^{\text{seg}} \cdot (T^{\text{s}} - T^{\text{ep}}) \qquad [50]$$

where $\lambda^{\text{ep,cell}}$ is the average thermal conductivity between end-plate and cell, $d^{\text{cell}-\text{ep}}$ is distance between the center of the end-plate and the cell segment, A^{seg} is the contact area between cell segment and end-plate segment, and T^{s} is the solid temperature of the neighboring cell segment.

Conductive heat flux is considered in the along-the-channel coordinate:

$$\dot{Q}^{\text{ep,ch}} = \dot{Q}_{\text{down}}^{\text{ep}} + \dot{Q}_{\text{up}}^{\text{ep}} \qquad [51]$$

The heat flux to the top and bottom segment of the end-plate respectively is calculated according to Fourier's law:

$$\dot{Q}_{\text{up}}^{\text{ep}} = \frac{\lambda^{\text{ep}}}{l_{\text{seg}}^{\text{ep}}} A^{\text{ep,cs}} \cdot (T_{\text{up}}^{\text{ep}} - T^{\text{ep}}) \qquad [52]$$

$$\dot{Q}_{\text{down}}^{\text{ep}} = \frac{\lambda^{\text{ep}}}{l_{\text{seg}}^{\text{ep}}} A^{\text{ep,cs}} \cdot (T_{\text{down}}^{\text{ep}} - T^{\text{ep}}) \qquad [53]$$

λ^{ep} is the thermal conductivity of the end-plate in along-the-channel coordinate, $l_{\text{seg}}^{\text{ep}}$ is the length of a segment, which is given by $l_{\text{seg}}^{\text{ep}} = \frac{l^{\text{ep}}}{N_{\text{seg}}}$,

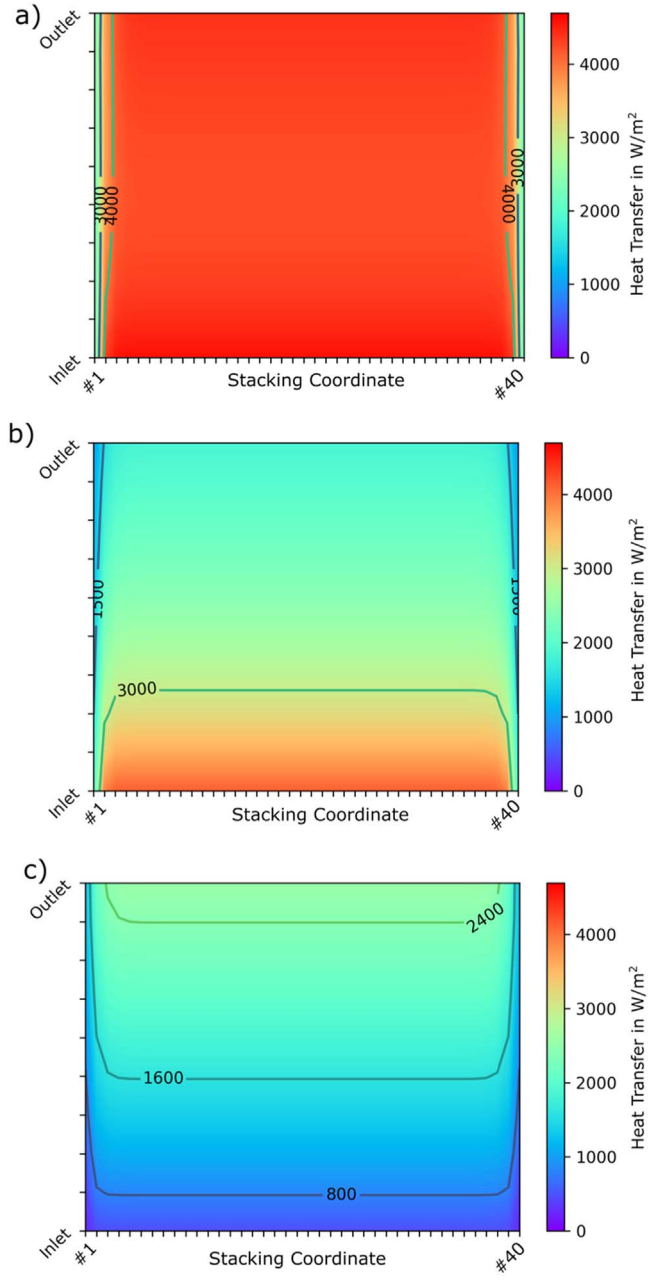

Figure 6. Heat transfer on the anodic side: (a) total heat transfer from solid to anodic fluid, (b) between solid and anodic liquid phase and (c) between solid and anodic gas phase at an average current density of 2.0 A cm^{-2}.

$A^{ep,cs}$ is the cross-sectional area of the end-plate orthogonal to the along-the-channel coordinate and $T^{ep}_{up/down}$ is the temperature of the neighboring segments along-the-channel. When setting these temperatures, the rules defined by Eqs. 45 and 46 are followed.

The end-plates are assumed to be thermally isolated against the surface on the bottom, whereas heat flux to the ambient is considered on the top:

$$\dot{Q}^{ep\to amb}_{eff} = \begin{cases} \dot{Q}^{ep\to amb}_{lat} + \dot{Q}^{ep\to amb}_{top} & \text{for segment at the top} \\ \dot{Q}^{ep\to amb}_{lat} & \text{for all other segments} \end{cases} \quad [54]$$

The convective heat transfer at the lateral surface is calculated with Eq. 55:

$$\dot{Q}^{ep\to amb}_{lat} = \alpha^{ep}_{lat} A^{ep}_{lat} \cdot (T^{ep} - T^{amb}) \quad [55]$$

where α^{ep}_{lat} is the heat transfer coefficient between the vertically erected surface of the end-plate and the ambient air and A^{ep}_{lat} is the lateral surface of the end-plate's segment, and T^{amb} is the temperature of the ambient air.

The convective heat flux from the horizontal surface at the top of the end-plates is considered:

$$\dot{Q}^{ep\to amb}_{top} = \alpha^{ep}_{top} A^{ep}_{top} \cdot (T^{ep} - T^{amb}) \quad [56]$$

where α^{ep}_{top} is the heat transfer coefficient for top surface and A^{ep}_{top} is the horizontal surface area at the top of the end-plate.

Stack.—The stack consists of cells and end-plates. The end-plates are thermally connected with the boundary cells. Charge and mass balances are formulated to connect the cells with each other. Unlike in most of the above section, indexing is needed at this point since the stack's cells and their segments are referenced for formulating the following balances.

Energy balances.—The stack model contemplates the energy balances formulated within the segment, cell, and end-plate model by assigning the neighboring segments' temperatures in stacking coordinate. This requires case distinction for the boundary cells since they are in direct contact with the two end-plates. Assigning the temperatures in stacking coordinate for Eqs. 4–5 for every cell segment gives:

$$T^{s}_{k,left} = \begin{cases} T^{ep}_{j,1} & \forall\, j \in \{1,\ldots,N_{seg}\} \wedge k = 1 \\ T^{s}_{j,k-1} & \forall\, j \in \{1,\ldots,N_{seg}\} \wedge k \in \{2,\ldots,N_{cells}\} \end{cases} \quad [57]$$

$$T^{s}_{k,right} = \begin{cases} T^{s}_{j,k+1} & \forall\, j \in \{1,\ldots,N_{seg}\} \wedge k \in \{1,\ldots,N_{cells}-1\} \\ T^{ep}_{j,2} & \forall\, j \in \{1,\ldots,N_{seg}\} \wedge k = N_{cells} \end{cases} \quad [58]$$

For the end-plate the reference temperatures in Eq. 50 are tied to their neighboring cell temperatures. The left end-plate's neighbor is cell 1, the right end-plate's neighbor is cell N_{cells}.

Charge balances.—Since the cells are connected in series, each cell receives the same current:

$$I^{stack} = I^{cell}_{k}\ \forall\ k \in \{1,\ldots,N_{cells}\} \quad [59]$$

The voltage of the stack is the sum of cell voltages:

$$U^{stack} = \sum_{k}^{N_{cells}} U^{cell}_{k}\ \forall\ k \in \{1,\ldots,N_{cells}\} \quad [60]$$

Mass balances.—The mass flow $\dot{m}^{\gamma,stack}_{in}$ into the γ-side of the stack is distributed equally to the first segment of each cell:

$$\dot{m}^{\gamma,cell}_{1,k,in} = \frac{1}{N_{cells}} \dot{m}^{\gamma,stack}_{in}\ \forall\ k \in \{1,\ldots,N_{cells}\} \quad [61]$$

At the stacks anodic and cathodic inlets only liquid water exists. In Eq. 61 a co-flow setup, where anode and cathode are cooled by an incoming water flow at the bottom of the stack, is described. For a counter-flow setup, this relation needs to be adopted.

The stack's anodic and cathodic outlet mass flow $\dot{m}^{\gamma,stack}_{out}$ is the sum of the cells' individual outgoing mass flows:

$$\dot{m}_{out}^{\gamma,stack} = \sum_{k}^{N_{cells}} \dot{m}_{k,out}^{\gamma,cell} \; \forall \; k \in \{1, \ldots, N_{cells}\} \qquad [62]$$

Validation and calibration.—The model is validated with experimental data from an industrial stack. The measured water mass-flow-rates into the stack (anode and cathode), the inlet temperatures and the stack current are used as model input variables. The cell voltages are used to calibrate the model and the outlet temperatures of the anode and cathode are used for validation.

A fitting algorithm (Python package lmfit[30]) is used to minimize the deviation between simulated and measured voltages by fitting the following parameters within physically reasonable boundaries: $i_0^{a,ref}$, $\alpha_{ct}^{a,ref}$, K^{mem}, E^{acd}, E^{mem}.

The fitted values are not published for confidentiality reasons of the industrial product. For the result section of this work, literature parameters are used (cf. Table I). Similarly, geometric and the remaining physical parameters are assigned generic values as shown in Table I.

However, the calibrated parameters lead to a good match between measured and simulated cell voltages for all cells under different operating conditions (cf. Fig. 2). Furthermore, the simulated outlet temperatures agree with the measured temperatures (cf. Fig. 2b), even though the temperatures were not used for model calibration, which indicates a good agreement of the implemented temperature model of the stack. Figure A·3 in the Appendix shows the simulation results and the deviations between simulated and measured data for the parameters given in Table I.

The stack is discretized in 40 cells and 10 segments per cell, whereas further discretization does not lead to significant quantitative changes of the results.

Results

First, temperature profiles and their influence on performance inhomogeneities are shown. This is followed by a study on how to influence and reduce those inhomogeneities. Focus is on varying water inlet flow rates, operating pressures, and counter-flow operation. For the following results, the inlet temperature is set to 60 °C for both, the anode, and the cathode side. In the base scenario both sides are provided with 0.15 kg $s^{-1}m^{-2}$ of process water flow in co-flow at a pressure of 1.0 atm.

Temperature profiles.—The contour plots in Figs. 3a and 3b display the temperatures of the solid and anodic fluid at a current density of 2.0 A cm^{-2} across both geometric dimensions considered in the model: The stacking coordinate on the x-axis and the along-the-channel coordinate on the y-axis. In Fig. 3a, the solid temperature profile is symmetric in stacking coordinate with colder temperatures at the boundary cells on the left and right side, than in the middle cells. This is due to cooling of the end-plates by free convection. The solid heats up along-the-channel from the bottom to the top because of the flow direction of the fluid. Heat is generated through voltage losses (cf. Eq. 12) within the solid, which then heats the fluids. Additionally, heat conduction between different cells in the stacking coordinate and segments in the along-the-channel coordinate occurs through the solid.

The temperature field of the anodic fluid in Fig. 3b has a similar shape as the temperature field of the solid in Fig. 3a. The fluid temperature is slightly below the solid temperature. The fluid is heated along-the-channel, which is more pronounced in middle than in boundary cells. Two opposing effects occur in the fluid phase. Firstly, it is heated through the solid via heat transfer. Secondly, the fluid is cooled because of water evaporation in the evolving gas-phase.

As the temperature fields change with the average current density, temperatures at different points inside the stack are plotted vs the average current density in Fig. 3c. As seen previously in Figs. 3a and 3b middle cell temperatures are higher than boundary cell temperatures at the inlet and outlet, respectively. Furthermore, temperatures increase with current density for both, fluid and solid. The solid temperature at the inlet increases slightly with increasing average current densities, because of heat conduction from the warmer middle parts of the cell.

At low average current densities up to 1.25 A cm^{-2}, boundary cells are generally cooler at the outlet than at the inlet, because of direct thermal coupling with end-plates, which are thermally connected to the environment. There, the cooling effect through the end-plate is larger than the heat generation inside the cell and heat conduction from inner cells. This cooling effect decreases and finally distinguishes going from the boundary cells to the middle cells.

The temperature differences between fluid and solid vary with current density, as it can be seen in Fig. 3d. The cool down of the end-plates can be seen in Fig. 3d as well, where the temperature differences $T^s - T^a$ are plotted for the same locations as in Fig. 3c. For boundary cells, the solid temperature is lower than the fluid temperature up to average current densities of 1.25 A cm^{-2}. For larger average current densities, the solid temperature is higher than the anodic fluid temperature. The heat flux from fluid to solid reverses and from there on, the fluid is cooler and heated by the solid materials of the cells. In the middle cells, the solid temperature is always higher, because of the negligible cooling effect of the end-plates.

Current density distribution.—Inside a cell, locally higher temperatures lead to locally reduced losses, which lead to higher current densities. This also induces the elevated generation of heat. The temperature field in Fig. 3a and the current density field in Fig. 4a interact: The current density field adapts to the temperature profile. At an average current density of 2.0 A cm^{-2}, it is more uniform in the boundary than in the middle cells. In the middle cells, the current density is 0.20 A cm^{-2} or 10% higher at the outlet than at the inlet of the cells. As the cell voltage is uniform through a cell, while the activation overpotentials and membrane resistance decrease with temperature, higher current densities appear in regions with higher temperatures throughout a cell. This leads to a more uniform current density in boundary cells due to a more homogenies temperature and vice versa for the middle cells.

The above-mentioned effects are coupled, such that locally higher temperatures lead to locally higher current densities, which again lead to locally larger heat generation. However, the main effect is the locally higher temperature as visualized in Fig. A·4) and Fig. A·5) which show that the nonlinear contributions of the heat generation have a low impact on the current density and temperature field.

The current density inhomogeneity shown in Fig. 4a exemplary for an average of 2.0 A cm^{-2} varies with the average current density. In Fig. 4b, the percentage difference between the inlet and outlet current density for the boundary and a representative middle cell is shown for varying current densities.

Unless the average current density is close to zero, for the middle cell the current density at the outlet is higher than the current density at the inlet with an almost linear increase of the difference up to 13.5% at an average current density of 2.5 A cm^{-2}. The reason is the heating of the cell from bottom to top. In the boundary cells, the outlet current density can be lower than the inlet current density for low to moderate average current densities up to 1.11 A cm^{-2}, e.g. at a very low average current density, the difference can increase up to −10.2%. However, the absolute difference of the current density from the average current density is much more pronounced for larger current densities. This is especially relevant since the typical operating range of industrial scale PEM electrolyzers lies in between 1.0 A cm^{-2} and 2.0 A cm^{-2} [6]. Current densities much lower are only present in start-up and shut-down scenarios. A longer operation at low current-densities is typically not feasible due to hydrogen cross-over from the cathode to the anode. The data presented in this

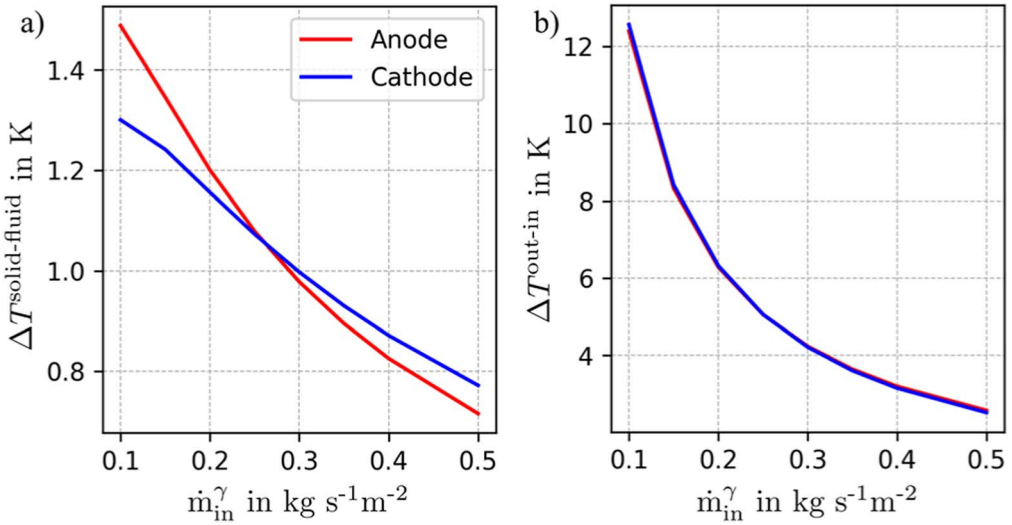

Figure 7. Influence of water flow rate on: (a) temperature difference between solid and fluid (b) temperature difference between outlet and inlet.

contribution is showing steady state results and are not fully validated at low current densities.

At an average current density of 1.11 A cm^{-2}, the current density at the outlet is as high as at the inlet. Compared to Fig. 3c, this is the same current density at which the outlet temperature equals the inlet temperature of the boundary cell, providing a uniform temperature and thus almost homogenous current density distribution along the cannel. With average current densities above 1.11 A cm^{-2}, the local current density at the outlet is also higher than at the inlet for all cells.

In summary, the inhomogeneities are greatest in the boundary cells at low current densities and in the middle cells at high current densities. Since in typical industrial stacks the number of cells within a stack is large, the effects of the middle cells must be considered to a special degree.

Polarization behavior.—Temperature and current density profiles lead to differences in cell voltages. Fig. 5 shows the different polarization behavior depending on the stacking coordinate.

In Fig. 5a only the stacking coordinate is shown, in which the average current density is constant for all cells. Due to lower temperatures at outer cells, the polarization behavior of outer cells is inferior, which is shown by tub shaped voltages for larger current densities. These lower temperatures lead to higher voltage losses mostly because of activation overpotentials and ionic membrane losses. Since the heat generation is modeled to be in the combined solid, the U-shaped voltages shown are symmetric as the temperatures. As described in the model section, in the along-the-channel coordinate the cell voltage does not vary because of the high electrical conductivity of the bipolar plates. The local contributions of the temperature dependent loss mechanisms to the cell voltage however vary and are shown for an average current density of 2.0 A cm^{-2} in Fig. A·6).

In Fig. 5b polarization curves for different cells (solid lines) and their deviations from the average stack polarization (dashed lines) are shown. The deviations in polarization behavior increase with increasing current densities. This is due to increased temperature gradients over the stack- and the flow-coordinate. For an average current density of 2.0 A cm^{-2} cell voltage differences between an inner and an outer cell of around 9 mV are calculated, which is a difference in voltage efficiency of 0.35%, as it is shown in A·5.

Heat transfer.—Performance, polarization, and some degradation mechanisms are mainly driven by the temperature of membrane and electrodes which is reflected in the solid temperature in this model. The temperature fields depend among other on heat transfer between solid and fluid.

To understand the heat transfer and its dependencies on the gas phase content, the heat transfer from solid to anodic fluid is plotted in Fig. 6. In Fig. 6a the total heat transfer is shown. Figures 6b and 6c show the effective contribution to the heat transfer from solid to the liquid and gas phase, respectively, so that Figs. 6b and 6c sum up to Fig. 6a, as it is stated in Eq. 8.

The total heat transfer to the fluid in Fig. 6a is higher in the middle cells, as compared to the end-plate-cooled boundary cells, because higher temperature differences between solid and fluid phase arise. A slightly decreased heat transfer from the inlet to the middle in direction of fluid flow is caused by a decreased liquid phase with a higher heat transfer coefficient. Closer to the outlet, heat transfer increases because of the velocity effect of the heat transfer coefficient (cf. Ep. (11)). At this point, it must be stated again, that the assumed heat transfer model is based on limited literature and needs further understanding.

The higher heat transfer at the inlets in Fig. 6b is caused by the high liquid volume fraction (1.0 at inlet, 0.07 at outlet). The heat transfer to the gas phase in Fig. 6c is lower than to the liquid phase, because of the lower transfer coefficient between solid and gas phase. It is counteracted towards the outlet by increasing fluid velocity (0.17 m s^{-1} at inlet and 1.21 m s^{-1} at outlet), such that the total heat transfer has limited variation along the channel in Fig. 6a.

Reduction of inhomogeneities.—Reducing the inhomogeneities is beneficial in two regards:

1. Performance can be increased by increasing the average cell temperature without exceeding temperature limitations, or the necessary mass flow for cooling can be reduced.
2. Degradation processes are distributed more homogeneously over the cell/stack since the rate of degradation among other factors, depends on temperature and load.[31]

Additionally, for aged stacks even higher inhomogeneities in temperature and polarization are implied, because of increased local voltages losses and resulting higher local heat generation.

To reduce the temperature differences the following three approaches are possible:

–Varying inlet water mass flow
–Varying operating mode (counter flow, pressure)

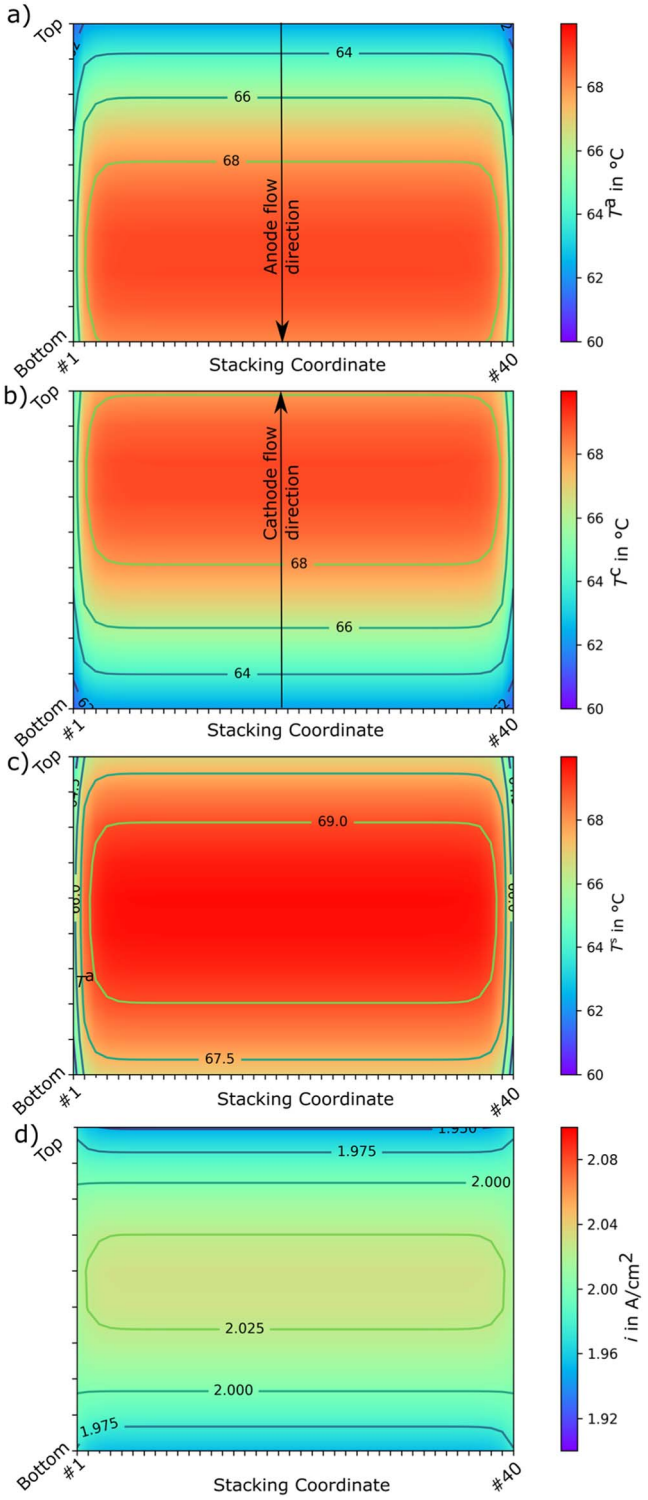

Figure 8. Temperature profiles and current densities in counter-flow operation. Anodic flow from top to bottom; cathodic flow direction remains from bottom to top: (a) anodic fluid temperature (b) cathodic fluid temperature (c) solid temperature and d) resulting current density distribution in stack.

–Structural changes (e.g., thermal insulation of end-plates, structure of PTL)

In the following the effects of changing the water mass flow, changing operation from equally oriented flow on anode and cathode to counter-flow, and different operating pressures are analyzed in detail.

Water mass flow.—The inlet water flow rate directly affects the outlet temperature of a stack as well as the temperature difference between solid and fluid. Due to higher mass flow through the stack the heat transfer is increased, and fluid and solid temperatures are lowered as shown in Fig. 7).

The higher flow rate leads to higher liquid fraction and to a higher mean velocity of the fluid, which is elevating the heat transfer coefficients between fluid and solid. Therefore, temperature differences between solid and fluid decrease with increasing flow rate, for water flow rates ranging from 0.025 kg s^{-1}m^{-2} to 0.5 kg s^{-1}m^{-2} at 1.0atm and $T_{in} = 60$ °C. As a rule of thumb for the considered flow rates, it can be stated that doubling the water flow rate cuts the temperature difference between inlet and outlet in half, as convective heat transport dominates the overall stack cooling. The effect on the temperature difference between solid and fluid is also causing a reduction but by a much magnitude. In general, this reduced temperature differences lead to a more homogenous operation. Quantitative details are discussed in Ch. 3.5.4.

Counter-flow.—In this section, the effect of a counter-flow operation, different flow directions of cathode and anode, is investigated. In this example the cathodic flow direction remains as in the examples above, from top to bottom but the water flow direction on the anode is reversed such that the process water enters the stack from top to bottom. Quantitative comparisons between co-flow and counter-flow operation are discussed in Ch. 3.4.5.

In Fig. 8a the anodic fluid temperature is shown, where the effect of the end-plate cooling again leads to cooler outer cells. In contrast to the temperature profiles of the fluids shown in Fig. 3b the temperature increases only up until around ¾ of the flow path and after that slightly decreases. This is because of the cooling effect of the water entering the cathode side with lower temperatures. The maximum temperature of the anodic fluid however is 1.0 K higher compared to the co-flow operation shown before. The same mechanism applies to the cathode, just flipped upside-down because of the fluid flow direction, Fig. 8b. The maximum fluid temperature is found 0.8 K higher than in the co-flow arrangement.

In Fig. 8c the solid temperature is shown. Here, the highest temperatures in along-the-channel direction are seen in the middle of the stack with lower temperatures at the bottom and top of cells. This is due to the cooling of the anodic fluid at the bottom and the cathodic fluid cooling at the top. Compared to the co-flow the observed solid temperature differences are lower inside the cells (cf. Fig. 3a). This is due to the additional solid heat transfer imposed by the cold fluid being supplied at different locations.

Figure 8d shows the resulting current density inhomogeneity. The deviations from the average current density in inner cells are still larger than in boundary cells. In comparison to the co-flow operation, the inhomogeneity has been reduced such that the current density ranges from 1.95 to 2.03 A cm^{-2} (compared to 1.90 to 2.10 A cm^{-2} in co-flow).

Operating pressure.—Another way to influence inhomogeneities is to vary the operating pressure. Among other effects, increasing the pressure leads to smaller volume fractions of product gas, which increases the heat transfer from solid to fluid and to higher reversible cell voltages. This affects the heat generation. Also, less water is evaporated, which reduces the evaporation enthalpy. Decreased fluid velocity leads to prolonged residence time of the fluid inside the cell but also reduces heat transfer. To examine those interconnected effects, the operating pressure is varied between 1.0 and 75 atm (cf. Fig. 9) with constant inlet mass flow rates of 0.15 kg s^{-1} m^{-2} and 60 °C at an average current density of 2.0 A cm^{-2}.

In Fig. 9a the heat generation Q^{diss} is shown. It increases moderately with higher pressures because the difference of U^{cell} and U^{th} is increasing (cf. Ch. 2.1.3).

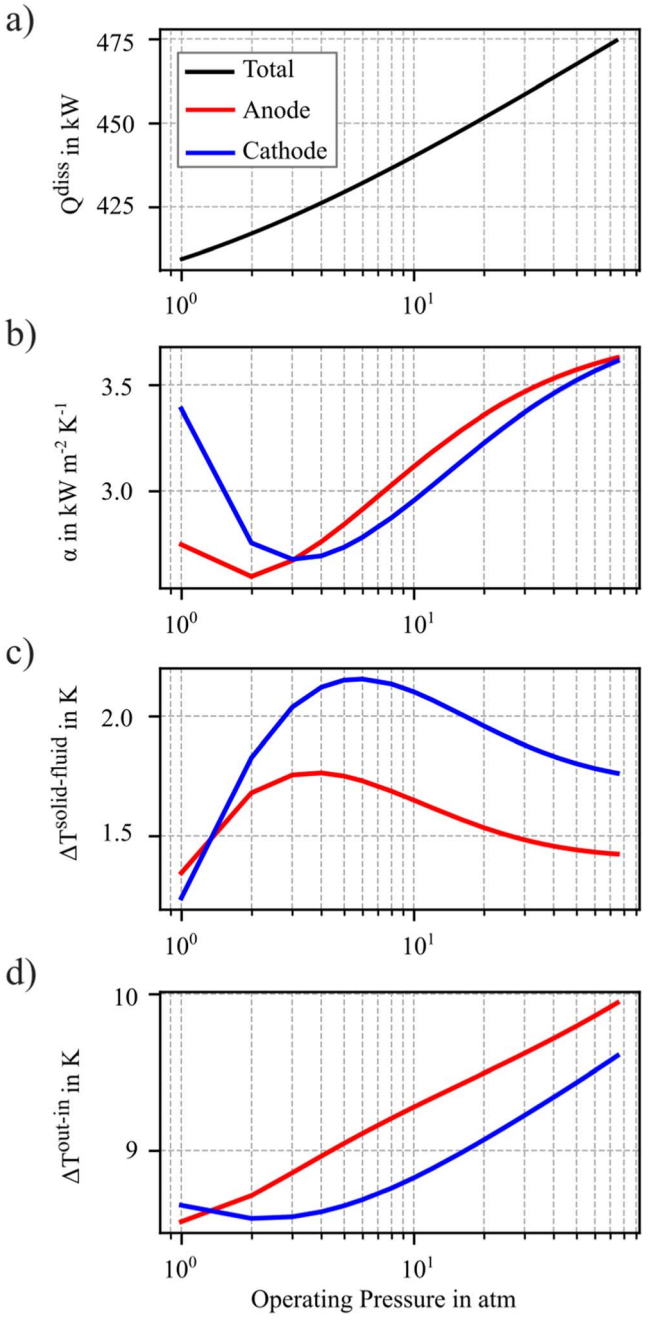

Figure 9. Influence of operating pressure on temperature differences: (a) total heat generation for given load, (b) avg. heat transfer coefficient for anode and cathode, (c) $\Delta T^{solid-fluid}$ at the outlet of an inner cell, and (d) ΔT^{out-in} of the anodic/cathodic fluid of the stack.

On the one hand, increased pressures lead to a higher volumetric liquid phase, which leads to a higher heat transfer coefficient. On the other hand, lower fluid velocities (lower volumetric gas phase with constant mass flow) lead to a decrease of the calculated heat transfer coefficients. These effects overlap in Fig. 9b, as the velocity effect dominates up until 2.0 atm on the anodic and 3.0 atm on the cathodic side and the high liquid phase dominates at high pressures.

In Fig. 9c the temperature difference between solid and fluid ($\Delta T^{solid \rightarrow fluid}$) determined by the heat transfer coefficients is shown. This difference initially increases until it reaches a maximum at 4.0 atm (anode) and 6.0 atm (cathode). Even beyond the maximum, the temperature difference on both, anode and cathode side remain

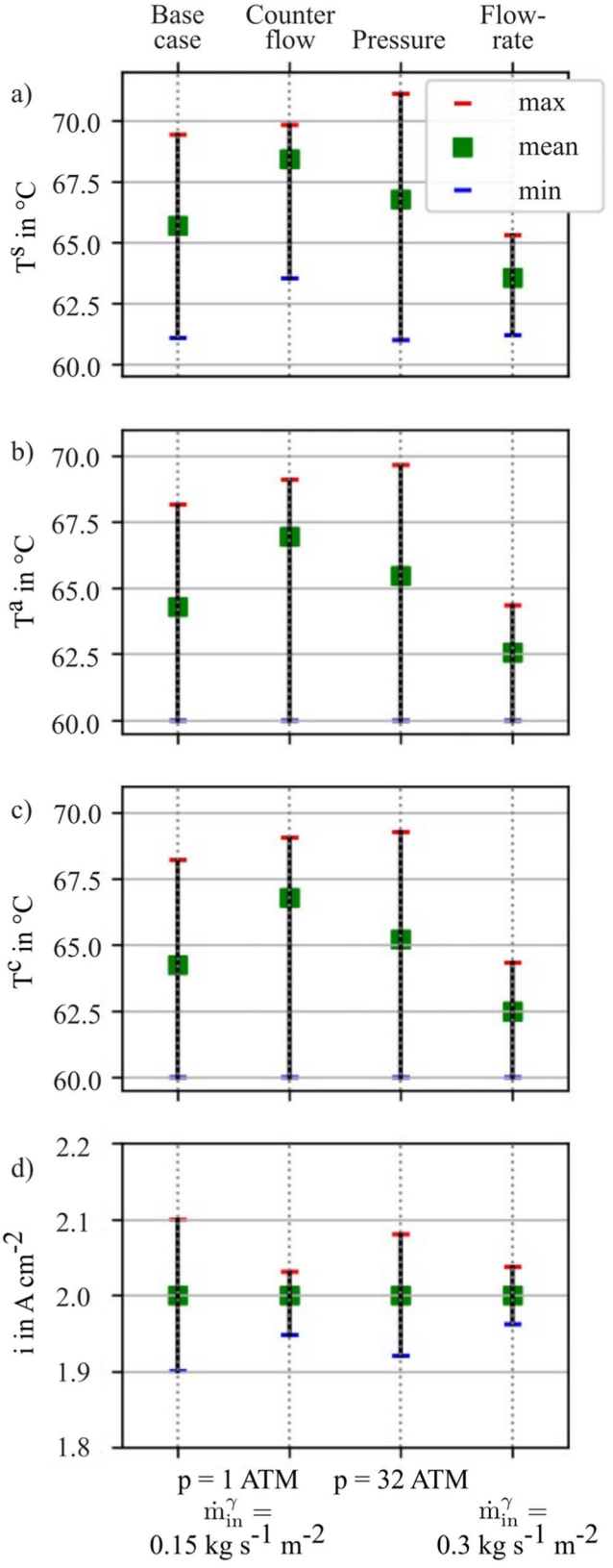

Figure 10. Impact of the different approaches (operating conditions) to reduce the inhomogeneities on: (a) solid temperature, (b) anodic fluid temperature, (c) cathodic fluid temperature and d) current density range inside the stack.

above the initial values for operation at 1.0 atm. The main reason for the net increase in $\Delta T^{solid \rightarrow fluid}$ for higher operating pressures is the increased generation of heat (Fig. 9a).

The temperature difference between outlet and inlet ($\Delta T^{\text{out}\rightarrow\text{in}}$) is shown in Fig. 9d. For the cathodic fluid the difference initially decreases slightly to a minimum at a pressure of 2.0 atm, which again corresponds to the pronounced drop of the heat transfer shown in Fig. 9b. However, for higher pressures, the increased heat generation, reduced evaporation rate, improved heat transfer and prolonged residence time lead to increased temperature differences.

Comparison of the different approaches.—In Fig. 10, the previously discussed approaches aiming to reduce the temperature and current densities inhomogeneities are compared. The base scenario is co-flow with inlet water mass flow of 0.15 kg s^{-1} m^{-2} on anode and cathode, operating pressure of 1.0 atm, and inlet temperatures of 60 °C.

For the solid temperature in Fig. 10a, the largest temperature ranges can be observed with pressure operation. While the base case with co-flow operation is having almost the same temperature difference as pressure operation, counter-flow and especially higher water mass flow significantly reduce the temperature span. For the counter-flow case, the average solid temperature is relatively close to its maximum, because of the large region of temperatures in the middle of the stack (cf. Fig. 8). This needs to be considered in the temperature control strategy of the stack.

The impact on the fluid temperatures on the anodic side in Fig. 10b and cathodic side in Fig. 10c is similar for both half-cells. The highest effects for decreasing the inhomogeneity of the solid temperature in Fig. 10a can be seen for the elevated water mass flow case. In the counter-flow case, the difference increases slightly. In regards of reducing the inhomogeneity high pressure operation does not have any positive effects.

The current density range in Fig. 10d depends on the solid temperature range in Fig. 10a. Therefore, higher solid temperature homogeneity indicates higher current density homogeneity. High reduction of current density inhomogeneity is achieved through both, the counter-flow operation and elevated water mass flow. The effect of pressure operation is negligible small, but still in a negative manner with increased inhomogeneity.

Both, counter-flow operation, and high mass flows gain higher homogeneity in the current density. For counter-flow and high-pressure operation, different stack designs are necessary. For elevated mass flows, higher pumping power is needed, which reduces the efficiency on a system level. In cases where the temperature fields show decreased maximums, this reduced efficiency can be mitigated by increasing the temperature of the water entering the stack.

Conclusions

A pseudo-2-D stack model consisting of coupled temperature and performance models was implemented and validated with industrial data. For confidentiality, however, this industrial data was not used for detailed quantification. Literature based parameters are in good quantitative agreement and used instead.

The heat transfer from solid to fluid is very important, but for a two-phase fluid mixture in porous layers of electrolyzers very little experimental data or theoretical relations is available for quantification. We presented a simple approach resolving heat transfer with respect to contributions from solid to liquid, from solid to gaseous media, and covering the effect of fluid velocity.

Temperature inhomogeneities appear between the solid and the fluid ($\Delta T^{\text{solid}\rightarrow\text{fluid}}$ for anode and cathode), the outlet and the inlet ($\Delta T^{\text{outlet}\rightarrow\text{inlet}}$) and between inner and outer cells of the stack ($\Delta T^{\text{inner cell}\rightarrow\text{outer cell}}$). Temperatures increase in flow direction with the outer cells being colder than inner cells. For average current densities above 1.0 A cm^{-2} the solid temperatures exceed fluid temperatures, especially in the middle (in stacking direction, up to 1.5 K at 2.0 A cm^{-2}).

The inhomogeneity in solid temperature induces deviations in local current densities. For low current densities, the boundary cells have the highest relative inhomogeneity (−4% at an average current density of 0.50 A cm^{-2}). For moderate and high average current densities, the inner cells have the highest inhomogeneity of 10.0% at an average current density of 2.0 A cm^{-2}, resulting in local current densities from 1.9 A cm^{-2} at the inlet to 2.1 A cm^{-2} at the outlet.

Current density and temperature deviations should be kept small, because of uneven performances and their negative effects on degradation. Therefore, different approaches to reduce the inhomogeneity ($\Delta T^{\text{outlet}\rightarrow\text{inlet}}$ and $\Delta T^{\text{solid}\rightarrow\text{fluid}}$) are shown. The effects of varying inlet mass flows, operating pressures and changing from co- to counter-flow operation are analyzed for an average current density of 2.0 A cm^{-2}. Higher inlet mass flows can directly reduce $\Delta T^{\text{outlet}\rightarrow\text{inlet}}$ and $\Delta T^{\text{solid}\rightarrow\text{fluid}}$ but higher cost and effort for pumping needs to be considered. High pressure operation does not have a positive effect on inhomogeneities, in fact it tends to lead to larger inhomogeneities. Counter-flow operation reduces temperature differences of the solid and therefore the resulting deviations in current densities, whereas the maximum temperatures for fluids and solid increase slightly. For such alternative operation modes however, changes in stack design might be necessary.

The influence of inhomogeneities on degradation needs to be researched in future. Especially for degraded stacks, the inhomogeneities might increase further due to elevated cell voltages and elevated heat generation within the stack.

Acknowledgments

This work was funded by the by the BMBF (German Federal Ministry of Education and Research) under the reference numbers: 03HY122A and 03HY122G.

Contributions

T. Krenz: Model - development, implementation, testing, validation, evaluation; discussion of results; writing - original draft, review and editing. **O. Weiland:** Model - development, implementation, testing, validation, evaluation; discussion of results; writing - original draft, review and editing. **P. Trinke:** Model - development; discussion of results; writing - review and editing. **L. Helmers:** Research idea; model - development; discussion of results; writing - review and editing. **B. Bensmann:** discussion of results; writing - review and editing.

C. Eckert: Model - development, implementation; discussion of results; writing - review and editing. **R. Hanke-Rauschenbach:** Model - development; discussion of results; writing - review and editing.

Appendix

A·1. Lumped parameters.—The thermal equivalent conductivities are calculated with the thermal conductivities of the single layers of a cell. The used values for the different layers are given in Table A·I and a schematic of the cell is shown in Fig. A·1.

$$\text{Parallel: } \lambda^{(\text{cell,ch})} = \frac{\sum \lambda^{\text{layer}}\delta^{\text{layer}}}{\delta^{\text{cell}}} = 8.3\,\text{Wm}^{-1}\text{K}^{-1} \qquad [\text{A·1}]$$

$$\text{Series: } \lambda^{\text{cell,sc}} = \frac{\delta^{\text{cell}}}{\sum \frac{\delta^{\text{layer}}}{\lambda^{\text{layer}}}} = 7.56\ \text{Wm}^{-1}\text{K}^{-1} \qquad [\text{A·2}]$$

$\lambda^{\text{ep,cell}}$ is then calculated combining the properties of an end-plate and half a neighboring cell (see Fig. A·2).

$$\lambda^{\text{ep,cell}} = \lambda^{\text{cell,sc}} = \frac{\delta^{\text{cell}}}{\sum \frac{\delta^{\text{layer}}}{\lambda^{\text{layer}}}} = 7.56\ \text{Wm}^{-1}\text{K}^{-1} \qquad [\text{A·3}]$$

For the specific heat capacity of the cell, we took the value for titanium, since the cell is predominantly made of titanium. We are

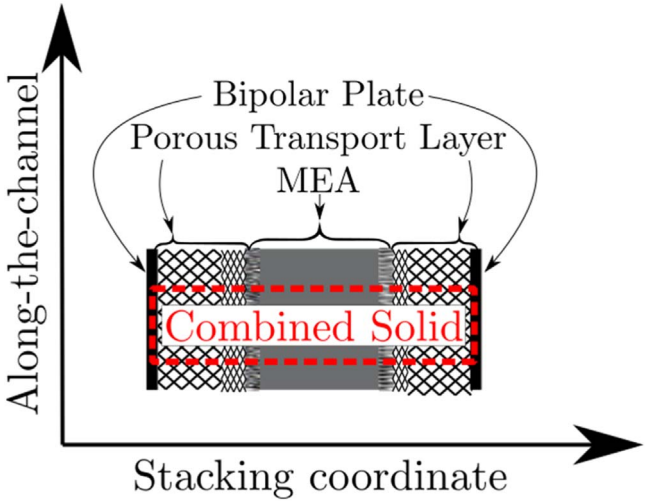

Figure A·1. Solid material as a combination of all layers of a cell: half of both bipolar plates, the PTLs and the MEA.

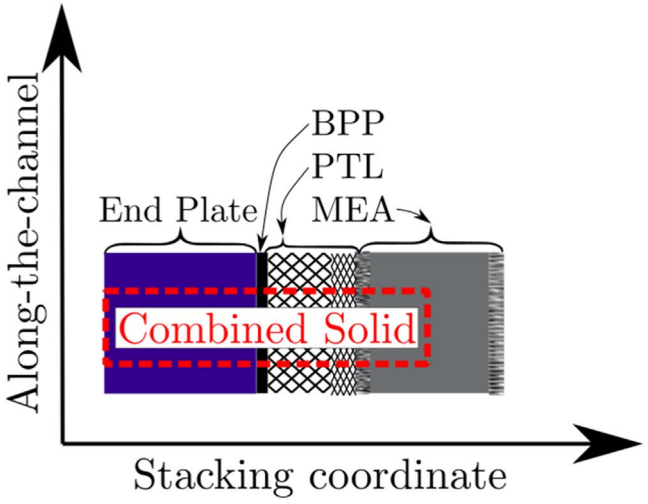

Figure A·2. Structure of end-plate and boundary cell.

showing steady state simulation results which are not affected by the chosen heat capacities. However, by using the values provided in Table A·II an averaged cell heat capacity c_p^{cell} can be calculated as follows:

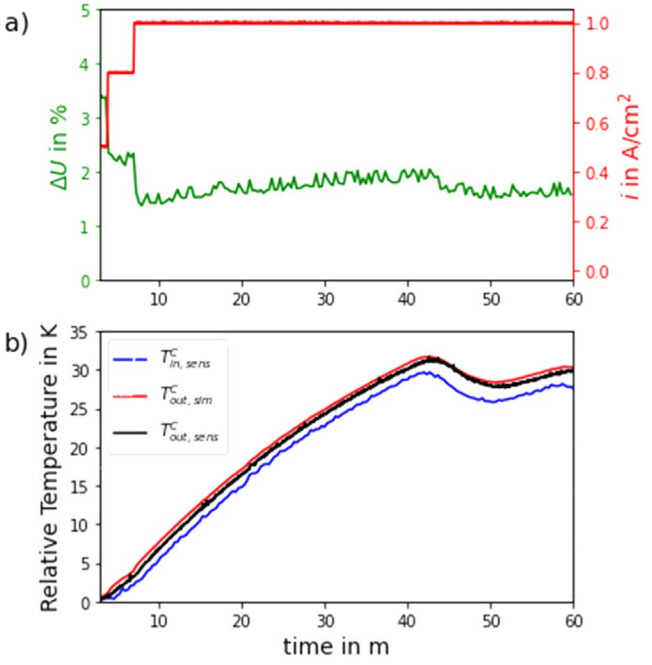

Figure A·3. Model validation at cold start of stack to partial load of 1.0 A cm^{-2} with literature parameters as provided in Table I: (a) current density (red) and relative error in simulated voltage $\Delta U = (U_{sim} - U_{sens})/U_{sens}$ in % (green) and (b) measured fluid temperature increase since cold start at inlet and outlet of cathode side ($T^c_{in,sens}$, $T^c_{out,sens}$) and corresponding simulated fluid temperature ($T^c_{out,sim}$).

$$c_p^{\text{cell}} = \frac{\sum c_p^{\text{layer}} \cdot m^{\text{layer}}}{m^{\text{cell}}} \qquad [A\cdot4]$$

A·2. Results of simulation with literature parameters.— Figure A·3 shows the simulation results based on literature parameters. The error is by one order of magnitude larger than with fitted parameters. However, the agreement with the measured average cell voltage of the stack is still given. The deviation in cell voltage leads to an error in the simulated outlet temperature. Since the simulated voltage is larger than the measured voltage the simulated outlet temperature exceeds the measured outlet temperature.

A·3. Temperature inhomogeneity drive current density inhomogeneity.—As stated in the result part of this work the current density distribution follows the temperature field. However, both

Table A·I. Thermal conductivities of layers in a cell.

Layer name	Thickness	Thermal conductivity	Material	Source
BPP (half)	1 mm	15 Wm^{-1}K^{-1}	Stainless steel	19
Anodic PTL	4.95 mm	7 Wm^{-1}K^{-1}	Titanium	32
MEA	0.1 mm	2.5 Wm^{-1}K^{-1}	Nafion	32
Cathodic PTL	4.95 mm	7 Wm^{-1}K^{-1}	Titanium	32
BPP (half)	1 mm	15 Wm^{-1}K^{-1}	Stainless steel	19

Table A·II. Thermal conductivities of cell and end-plate.

Layer name	Thickness	Thermal conductivity	Material	Source
Cell (half)	6 mm	7.56 Wm^{-1}K^{-1}	Mixed	Calculation: A·1
End-plate	50 mm	15 Wm^{-1}K^{-1}	Stainless steel	19

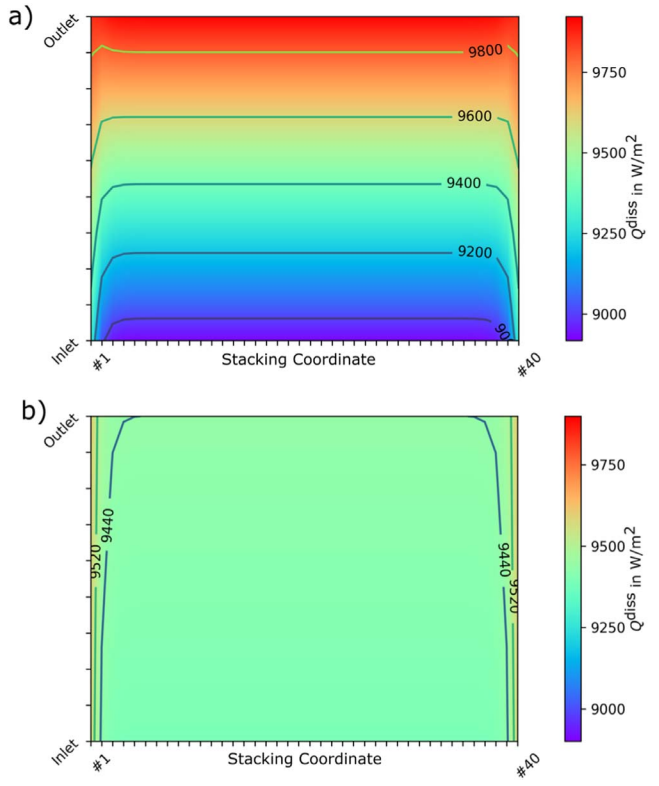

Figure A·4. Dissipation Heat Production in case of: (a) variable current density and (b) constant current density.

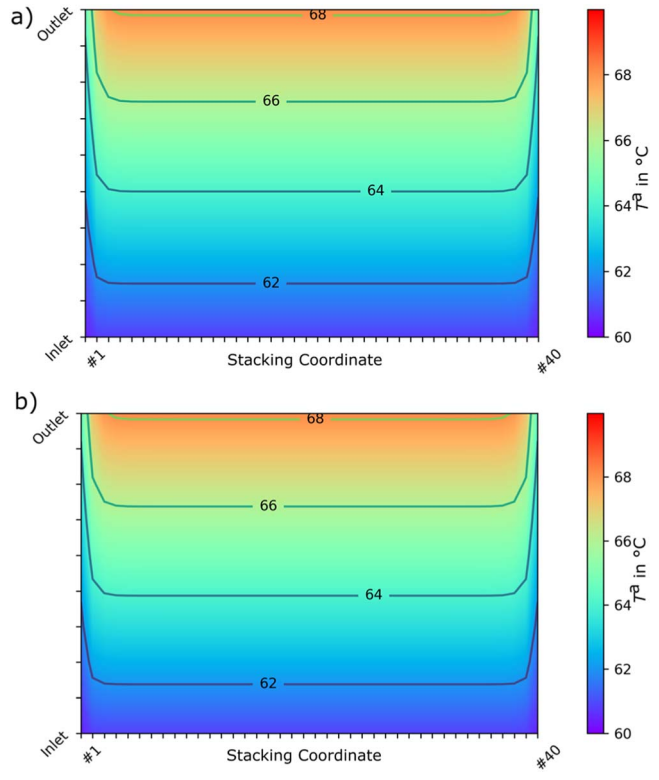

Figure A·5. Anodic fluid temperature in case of: (a) current density differences induced by temperature differences and (b) no deviations of segment current densities from average stack current density.

influence each other: a higher current density also leads to a higher heat generation and even though the thermos-neutral voltage is reduced for higher temperatures. Thus, one could also state that the current density distribution leads to the amplification of the temperature profile. However, the nonlinear heat generation effect is small.

The resulting effect is shown in Fig. A·4. To show the minor impact of the current density distribution itself on the temperature fields, in Fig. A·5 the heat generation is calculated using $i^{avg} = I^{stack}/N_{seg}$ in every segment. The effects on the temperature field are very small which is why the chain of causality is as described above (Fig. A·4).

A·4. Voltage loss mechanisms.— The voltage loss mechanisms depend a.o. on temperature and current density, so they contribute differently to the cell voltage in different positions within the stack depending on the local temperature and current density, as it is shown in Fig. A·6. Higher activation overpotentials are seen in the

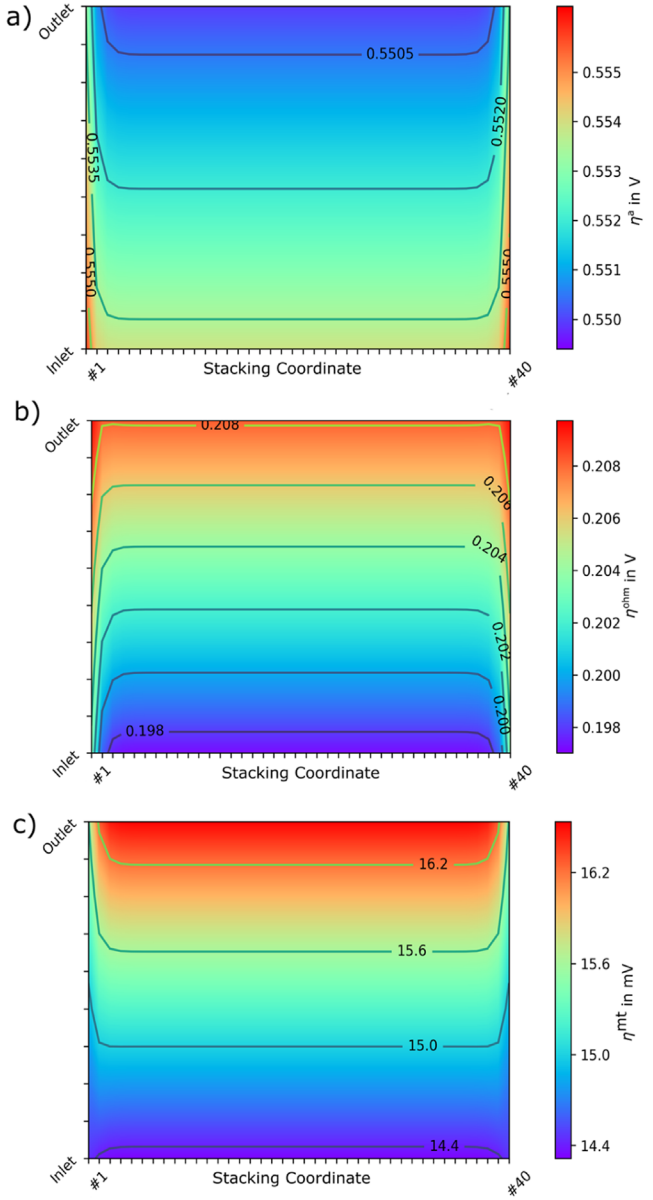

Figure A·6. Local voltage loss contributions at 2.0 A cm^{-2}: (a) activation overpotential, (b) ohmic overpotential and (c) mass transport overpotential.

cooler areas because of temperature effects, whereas the ohmic losses are higher in warmer areas because of higher current densities.

A·5. Voltage efficiency.—The voltage efficiency according to the higher heating value is calculated with the cell voltages and the thermo-neutral voltage:[7]

$$\epsilon_{\mathrm{V}}^{\mathrm{HHV}} = \frac{U^{\mathrm{thn}}}{U^{\mathrm{cell}}} \qquad [\mathrm{A}\cdot 5]$$

With $U^{\mathrm{thn}}(T = 60\ ^{\circ}\mathrm{C}) = 1.481\ \mathrm{V}$, $U_{\mathrm{inner}}^{\mathrm{cell}} = 1.97685\ \mathrm{V}$ and $U_{\mathrm{outer}}^{\mathrm{cell}} = 1.98610\ \mathrm{V}$, this leads to:

$$\Delta\epsilon_{\mathrm{V}}^{\mathrm{HHV}} = \epsilon_{\mathrm{V,inner}}^{\mathrm{HHV}} - \epsilon_{\mathrm{V,outer}}^{\mathrm{HHV}} = \frac{U^{\mathrm{thn}}}{U_{\mathrm{inner}}^{\mathrm{cell}}} - \frac{U^{\mathrm{thn}}}{U_{\mathrm{outer}}^{\mathrm{cell}}} = 0.349\% \qquad [\mathrm{A}\cdot 6]$$

ORCID

T. Krenz https://orcid.org/0000-0001-7170-1945
O. Weiland https://orcid.org/0000-0002-5135-1703
P. Trinke https://orcid.org/0000-0002-0935-5321
C. Eckert https://orcid.org/0000-0002-1266-8660
B. Bensmann https://orcid.org/0000-0001-8685-7192
R. Hanke-Rauschenbach https://orcid.org/0000-0002-1958-307X

References

1. M. Wappler, D. Unguder, X. Lu, H. Ohlmeyer, H. Teschke, and W. Lueke, *Int. J. Hydrogen Energy*, **47**, 33551 (2022).
2. A. Kovač, M. Paranos, and D. Marciuš, *Int. J. Hydrogen Energy*, **46**, 10016 (2021).
3. H. Ishaq, I. Dincer, and C. Crawford, *Int. J. Hydrogen Energy*, **47**, 26238 (2022).
4. A. I. Osman, N. Mehta, A. M. Elgarahy, M. Hefny, A. Al-Hinai, A. H. Al-Muhtaseb, and D. W. Rooney, *Environ. Chem. Lett.*, **20**, 153 (2022).
5. K. Zhang et al., *Nano Research Energy*, **1**, e9120032 (2022).
6. K. Ayers, N. Danilovic, K. Harrison, and H. Xu, *Electrochem. Soc. Interface*, **30**, 67 (2021).
7. D. G. Bessarabov, H. Wang, H. Li, and N. Zhao (ed.), *PEM electrolysis for hydrogen production: Principles and applications* (CRC Press, Boca Raton, FL) (2016).
8. M. Chandesris, V. Médeau, N. Guillet, S. Chelghoum, D. Thoby, and F. Fouda-Onana, *Int. J. Hydrogen Energy*, **40**, 1353 (2015).
9. Z. Abdin, C. J. Webb, and E. Gray, *Int. J. Hydrogen Energy*, **40**, 13243 (2015).
10. F. MARANGIO, M. Santarelli, and M. CALI, *Int. J. Hydrogen Energy*, **34**, 1143 (2009).
11. S. Siracusano, V. Baglio, N. Briguglio, G. Brunaccini, A. Di Blasi, A. Stassi, R. Ornelas, E. Trifoni, V. Antonucci, and A. S. Aricò, *Int. J. Hydrogen Energy*, **37**, 1939 (2012).
12. S. Shiva Kumar and V. Himabindu, *Materials Science for Energy Technologies*, **2**, 442 (2019).
13. K. Onda, T. Murakami, T. Hikosaka, M. Kobayashi, R. Notu, and K. Ito, *J. Electrochem. Soc.*, **149**, A1069 (2002).
14. C. Immerz, M. Schweins, P. Trinke, B. Bensmann, M. Paidar, T. Bystroň, K. Bouzek, and R. Hanke-Rauschenbach, *Electrochim. Acta*, **260**, 582 (2018).
15. P. Olivier, C. Bourasseau, and B. Bouamama, *IFAC-PapersOnLine*, **49**, 1014 (2016).
16. W. J. Tiktak, *Heat Management of PEM Electrolysis: A study on the potential of excess heat from medium- to large-scale PEM electrolysis and the performance analysis of a dedicated cooling system*, TU Delft (2019).
17. G. Correa, P. Marocco, P. Muñoz, T. Falagüerra, D. Ferrero, and M. Santarelli, *Int. J. Hydrogen Energy*, **47**, 4315 (2022).
18. R. Franke, F. Casella, M. Sielemann, K. Proelss, and M. Otter, "Standardization of Thermo-Fluid Modeling in Modelica.Fluid." *7th Int. Modelica Conference* (2009).
19. P. Stephan, S. Kabelac, M. Kind, D. Mewes, and K. Schaber (ed.), *VDI-Wärmeatlas: Fachlicher Träger VDI-Gesellschaft Verfahrenstechnik und Chemieingenieurwesen* (Berlin, Springer) (2019).
20. T. E. Springer, T. A. Zawodzinski, and S. Gottesfeld, *J. Electrochem. Soc.*, **138**, 2334 (1991).
21. Q. Duan, H. Wang, and J. Benziger, *J. Membr. Sci.*, **392-393**, 88 (2012).
22. M. Suermann, T. J. Schmidt, and F. N. Büchi, *ECS Trans.*, **69**, 1141 (2015).
23. H. Ito, T. Maeda, A. Nakano, and H. Takenaka, *Int. J. Hydrogen Energy*, **36**, 10527 (2011).
24. K. J. Laidler, *J. Chem. Educ.*, **61**, 494 (1984).
25. R. García-Valverde, N. Espinosa, and A. Urbina, *Int. J. Hydrogen Energy*, **37**, 1927 (2012).
26. B. Han, S. Steen, J. Mo, and F. Zhang, "Modeling of Interfacial Resistance Effects on the Performance and Efficiency for Electrolyzer Energy Storage." *13th International Energy Conversion Engineering Conference* (2015).
27. P. Trinke, G. P. Keeley, M. Carmo, B. Bensmann, and R. Hanke-Rauschenbach, *J. Electrochem. Soc.*, **166**, F465 (2019).
28. P. Trinke, B. Bensmann, and R. Hanke-Rauschenbach, *Int. J. Hydrogen Energy*, **42**, 14355 (2017).
29. H. Wu, X. Li, and P. Berg, *Int. J. Hydrogen Energy*, **32**, 2022 (2007).
30. M. Newville, T. Stensitzki, D. B. Allen, and A. Ingargiola, "LMFIT: non-linear least-square minimization and curve-fitting for python." *Zenodo* (2014).
31. F. Fouda-Onana, M. Chandesris, V. Médeau, S. Chelghoum, D. Thoby, and N. Guillet, *Int. J. Hydrogen Energy*, **41**, 16627 (2016).
32. R. Bock, H. Karoliussen, F. Seland, B. G. Pollet, M. S. Thomassen, S. Holdcroft, and O. S. Burheim, *Int. J. Hydrogen Energy*, **45**, 1236 (2020).